MASS ANOMALY STRUCTURE OF THE EARTH

Carl Bowin
Department of Geology and Geophysics
Woods Hole Oceanographic Institution
Woods Hole, Massachusetts

Abstract. Gravitational interaction is the weakest among the four known forces in the universe. The particular gravity equipotential field that coincides with sea level is called the geoid, and satellite data have revealed anomalies in its pattern that are puzzling to explain. Dynamic topography solutions have offered the preferred explanation for the past 15 years, but problems remain. An alternative explanation presented here contends that very large mass anomalies lie deep in the Earth, presumably produced by topography at the core-mantle boundary (CMB), and only much smaller mass anomalies occur at shallower depths. The principal distinction is whether one is willing to accept the possibility that processes within the Earth's core may generate the CMB topography. An analysis of the South American regional geoid high (spherical harmonic degrees 2–10) indicates that only mass anomalies shallower than 1200 km are its cause. This single positive source is contrary to dynamic topography solutions that would generate negative deflections of both the surface and the CMB in response to the positive subducted mass for the Earth's fourth greatest geoid high. Our alternate explanation is tested utilizing a set of 9274 subduction 5° cube slab bloblet center points, developed from reconstructed plate history, that provide estimates of the locations of material subducted into the Earth's mantle. Two global mass solutions are offered utilizing (1) only those bloblets in the outer 800 km and (2) only those bloblets in the outer 1400 km. Four point masses at 3000 km depth to simulate CMB topography, produced by processes within the core unrelated to mantle dynamic topography, complete the two mass models. Both models show reasonable agreement with patterns and magnitudes of the regional geoid and its component degree parts. The model CMB mass anomalies are only a factor of 3 greater than those initially estimated by gravity to geoid ratios from observed values at geoid anomaly center locations. Difficulties with the dynamic topography solutions, matters of the density of the subducted material, the proper hydrostatic flattening value to use for analyses, and possible causes for the CMB topography are discussed. The subduction mass models are also used to estimate the magnitude of the driving force for plate tectonics (2.78×10^{20} to 3.23×10^{21} N), approximately equivalent to 7.0×10^{12} to 8.1×10^{13} N m^{-1}. These force values are comparable to published slab force estimates based on thermal considerations.

1. INTRODUCTION

Gravitational interaction is the weakest among the four known forces in the universe: electromagnetism, the strong force, the weak force, and gravity. The strong and weak forces are important at atomic and subatomic distances. Gravity, however, although weak, seemingly reaches out over great distances and has molded the observed patterns of galaxies and the arrangements and shapes of their constituents. To our normal senses it is the force that causes objects to fall to the ground at a rate that accelerates at 980 cm s^{-2} (~32 feet s^{-2}) because of the attraction from the mass of our planet. The same force keeps the Moon in orbit around our Earth. The gravitational attraction between two point masses appears to be only proportional to the product of those masses (Newton's law) and inversely to the square of their distance apart. However, when one or both of these masses becomes extremely great, and/or their velocity approaches that of the speed of light, other terms are then needed to account for the properties of gravity (such as Einstein's gravitational theory). The history of our understanding of gravity parallels that of many topics of scientific inquiry. Proclamations are made; evidence is discussed, rejected, or accepted; and new ideas and modifications are presented. For the last 15 years the concept of "dynamic topography" has been the accepted explanation for why anomalies in the Earth's geoid (Plate 1) have no obvious relationship to the planet's topography, magnetic anomalies, or plate tectonics. In this review, evidence is given that dynamic topography perhaps does not play the dominant role in contributing to the gravity field that it usually is assumed to. In addition, an alternate interpretation for the deep structure of the Earth is presented.

2. BACKGROUND

The "logical" fact that heavy objects fall faster than lighter objects was written (~340 B.C.) by Aristotle

8755-1209/00/1999RG000064$15.00

Reviews of Geophysics, 38, 3 / *August 2000*
pages 355–387
Paper number 1999RG000064

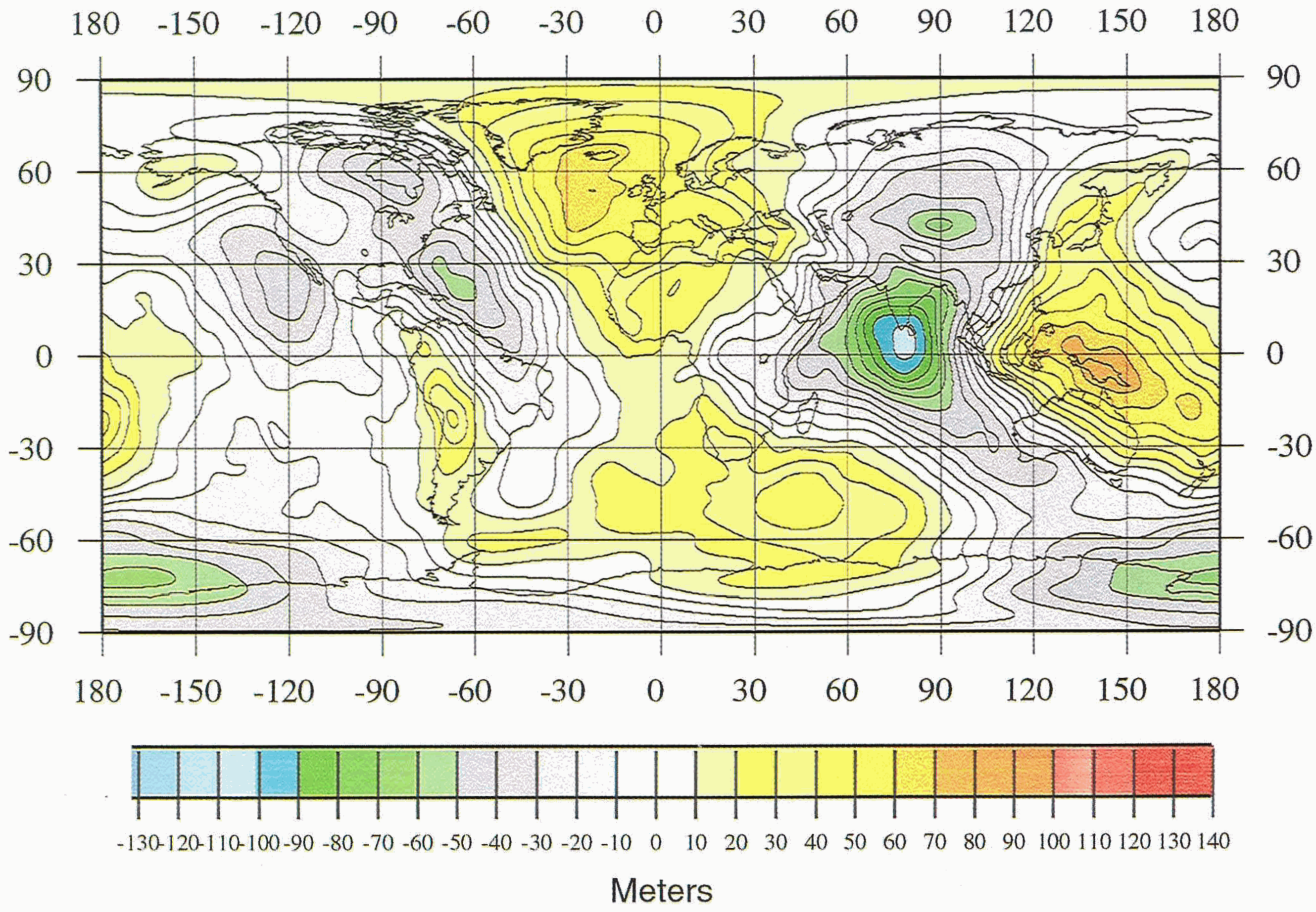

Plate 1. Earth's geoid anomaly map for spherical harmonic degree ranges 2–250. Computed Goddard Earth Model GEM-t2 coefficients [*Marsh et al.*, 1990] are referenced to ellipsoid with reciprocal flattening 298.257 (actual Earth flattening).

(384–322 B.C.), a pupil of Plato. Leonardo da Vinci (1452–1519) was the first to initiate new thinking about the physics of the Earth since that time. He observed that the speed of a falling body increases with time. However, it was not until about 1600 that Galileo Galilei (1564–1650) reasoned that air resistance had misled the Aristotelians. Galileo pointed out that dense objects, for which air resistance is relatively unimportant, fall almost together and that their motion is one of constant acceleration. Galileo confirmed his ideas by utilizing inclined surfaces to lengthen times of fall and pendulums with bobs made of different materials yet retaining the same period of swing. The unit of gravitational acceleration is named after him: 1 Gal = 1.0 cm s^{-2}. Sir Isaac Newton (1642–1727) came to argue (~1680) that a heavy object has more "stuff in it to be moved" than a light object. This greater "stuff," or matter, he came to call mass, has more "inertia" and needs more force for its acceleration. Thus the remarkable property of gravitation is that the Earth's pulls are proportional to the inertial mass of the matter pulled. Newton deduced the formula (to be presented later) for the force of gravitational attraction between two masses. He estimated the value of G, the gravitational constant, by assuming an average mass density for the Earth 5.5 times that of water, calculating a total mass of the Earth and rearranging his force equation. G, however, remained unmeasured for over 50 years after his death. Pierre Bouguer (1698–1790) compared the regional mass of the Earth with the local mass of a mountain by using pendulum measurements (1740). The correction for the mass of topography above a datum, commonly sea level, is now termed the "Bouguer correction," and the resulting anomaly after application of the correction is called the "Bouguer anomaly." Reverend John Mitchell (1724–1793) described a method for measuring the gravitational field by a "torsion balance" in 1777. Henry Cavendish (1798) put Mitchell's method into practice and was the first to determine G and thus the mass of the Earth.

In 1890, Baron Roland von Eötvös (1848–1919) completed his first single-beam torsion balance, a significant improvement over those built previously by Mitchell and Coulomb a century before. After conducting extensive field observations in Hungary, von Eötvös in 1902 invented his double-beam torsion balance. The use of a "gravity meter," by observing the displacement of a weight on a spring, was suggested in 1833 by Sir John Herschel. A device of this type that could achieve an accuracy comparable to that obtained by pendulums was not developed for more than a century. In 1817, Henry Kater began using a reversible pendulum for making absolute measurements of gravity. By determining the distance between two alternate points on a rigid pendulum bar that yield identical periods, he discovered that separation is equal to the length of an equivalent simple pendulum, therefore providing an absolute gravity observation. In 1872, Ernst Mach argued that acceleration, and hence inertia, is not absolute but only has meaning within a frame of reference.

During the 1930s, static gravimeters with elastic quartz fibers or metal springs (particularly the "zero-length spring" patented by Lucian LaCoste) replaced pendulums for local measurements over small ranges. In the 1960s they were extended to have a global range. In 1960, James Faller succeeded in monitoring the fall of a first-surface mirror in a vacuum chamber, using laser interferometry, to make an absolute gravity measurement. Since then, pendulums have been obsolete for both relative and absolute gravity observations. In the late 1950s and 1960s, static gravity meters were modified to allow conducting dynamic gravity measurements aboard ships. *Torge* [1989] describes a number of ship and airborne gravity measuring instruments. Gabriel Luther in 1986 determined the current benchmark value for the gravitational constant, G, to be 6.6726×10^{-11} m^3 kg^{-1} s^{-2}, but ongoing test measurements vary as much as 0.6% [*Regalado*, 1995]. *Rauch* [1993] cites results demonstrating connections between gravity and quantum fields using neutron interferometry. B. Haisch, A. Rueda, and A. Puthoff (in the paper by *Matthews* [1994]) have proposed that the seething quantum mechanical activity of the subelementary particle world that occurs even in a vacuum offers the resistance known as inertia. In 1999, cosmologists analyzing the irregularities in the cosmic microwave background, and finding a peak in power near 1° in the angular size of fluctuations, claim to have a complete accounting of the matter and energy of our universe and say it is "flat" (i.e., expanding with uniform acceleration so that parallel lines remain parallel) [*Sincell*, 1999]. Further, this requires that a major part of the total energy be in an unfamiliar form of energy (a mass equivalent) in empty space. $E = mc^2$ (the constant, c, the velocity of light, enters because it defines a limit: nothing can travel faster). This energy is presumed to arise from the vibrations of superstrings. The fundamental units of electrons, neutrinos, quarks, muons, and taus, as well as the messenger carriers of all four forces of the universe, arise from different vibration characteristics (M theory) [*Witten*, 1997]. The length of the vibrating superstrings is of the order of the Planck length: 10^{-33} cm. Presumably, the superstring's characteristic enormous vibrational Planck-scale energy (in a vacuum, for example) is very closely canceled at longer wavelengths by jitters of quantum uncertainty [*Greene*, 1999]. Superstring (M theory) theories predict time variation of G in some proportion to the universe's Hubble expansion rate, which is about 10^{-10} $year^{-1}$ [*Nordtvedt*, 1996].

Now that precise position and elevation are becoming more accurate by the Global Positioning System (GPS), continuous airborne and vehicle three-dimensional location measurements by differential interferometry are increasingly practical and advantageous. With the advent of artificial satellites orbiting the Earth, it has become practical to measure irregularities in the shape of the Earth's gravitational equipotential field, which is equivalent to the integral of the gravity field (and hence varies as $1/d$ rather than $1/d^2$, where d is distance). The equipotential field that coincides with sea level is called the geoid, and satellite data have revealed anomalies in its pattern that are puzzling to explain (Plate 1). Gravity equipotential (geoid) anomalies vary as inverse distance ($1/d$) and in the Earth are most diagnostic of large mass anomalies at depths of thousands of kilometers. Gravity anomalies vary as inverse distance squared (i.e., $1/d^2$) and are most sensitive to Earth mass anomalies within 100 km of the surface. Radar (or laser) altimeters directed downward from orbiting satellites provide observations of small-scale irregularities in the ocean geoid. There are two methods of estimating gravity anomalies from small-scale geoid irregularities provided by the altimeter data. One method is to deal with residual local geoid anomalies (after removal of a regional field) by computing a covariance function from data surrounding a selected location and then applying an appropriate transfer function. This was the method used for computing world residual geoid, gravity, and vertical gravity gradient maps by *Bowin* [1991, Figures 5 and 6]. A second method utilizes local variations in the horizontal gradient of the geoid to compute horizontal gravity variations and from them to estimate vertical gravity anomalies (or estimating bathymetry variations) [*Sandwell and Smith*, 1997]. A viable and reliable vertical gravity gradiometer or tensor sensor (varying as $1/d^3$) is awaited to improve detection and analysis of structures in the outer 10 km of the Earth (see Figure 1).

The most precise information regarding internal Earth structure is provided by study of Earth seismicity (earthquakes). Formal seismic instrumentation appeared as early as A.D. 132 when Chang Heng set up a seismoscope in China that indicated both the occurrence of an earthquake and its direction of first motion. Presently, the Federation of Digital Seismic Networks (FDSN) coordinates, maintains, and distributes acquired data to investigators worldwide. These data together with those from the Incorporated Research Institutions for Seismology (the IRIS consortium) and its subprogram the Global Seismic Network (GSN), as well as the recent Ocean Seismic Network (OSN) [*Stephen*, 1998], now provide global information utilized by seismic tomography solutions. These solutions are presently providing increasingly detailed three-dimensional images by seismic tomography of the P (compressional) and S (shear) wave structure of the Earth's mantle. In

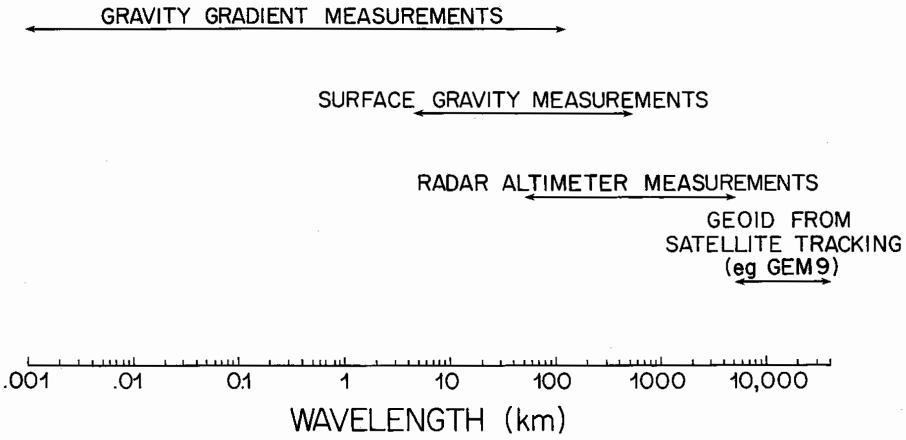

Figure 1. Wavelength bands where surface gravity, geoid from radar altimeter, and geoid from orbit perturbation measurements are considered most accurate. Logarithmic wavelength scale is used. Reprinted from *Bowin et al.* [1986] with permission.

turn, these seismic tomography solutions have become the input data sets for dynamic topography experiments in testing various conversions of seismic P and S velocity to density and the effects of viscosity variations with depth in the mantle. Such dynamic topography experiments then test their results by their ability to match the global geoid anomaly pattern (Plate 1).

3. GRAVITY AND GEOID

Whether gravity acts via curvature of a space-time field of our universe, or via massless graviton spin-2 messenger particles (or some other force unit) traveling at the speed of light among interacting masses, now may be gradually resolved by superstring theory [*Greene*, 1999]. In gravitational field theories each mass body is considered to form a surrounding gravitational field that permeates all surrounding space but weakens farther from the source. Other bodies in that surrounding space experience a force, and responses are produced, causing a superposition at all points in space of the gravitational fields due to all bodies in that space. Einstein's general relativity theory includes higher nonlinear terms in addition to the Newtonian term for gravitational acceleration:

$$A = -\frac{GMR}{R^3} + 2\frac{G^2M^2R}{c^2R^2} - \frac{3}{2}\frac{GMR}{R^2}\left(\frac{V^2}{c^2}\right) - \frac{V \cdot AV}{c^2} - \frac{1}{2}\frac{V^2}{c^2}A + \dots . \quad (1)$$

A is the acceleration vector of a moving particle of negligible mass, G is the gravitational constant, R is the distance vector from mass M, V is the particle's velocity vector, and c is the speed of light. Again, c appears because it is a fundamental limiting velocity for every quantity transporting real mass or energy. That velocity provides scaling terms on the relativistic effects in relation to the dimensions of G and V. Terms of higher power of $1/c$ are neglected. Objects must obtain velocities approaching that of light before the relativistic effects on space-time need be considered. Small deviations from the first Newtonian term have been detected in millisecond radio pulsars [*Taylor and Weisberg*, 1989; *van der Klis*, 1999]. The first term is related to Newton's law for the force of gravity between two masses:

$$F = \frac{GM_1M_2}{R_{12}^2}. \quad (2)$$

Remembering that force equals mass times acceleration, we see that the downward acceleration due to Earth's gravity on a mass at the Earth's surface (assuming the Earth to be a sphere) is

$$g = \frac{GM_e}{R_e^2} \quad (3)$$

and is equivalent to the first term in (1).

A gravity anomaly is defined as an acceleration of gravity that is greater or less than a mean value. Bathroom scales are not sensitive enough to detect the small variations in the weight of objects at different locations over the Earth's surface. Those weight differences arise because the acceleration of gravity due to the mass of the Earth varies. Some instruments, however, can measure these small variations in the local gravity acceleration associated with Earth gravity anomalies. Although there has been much progress in measuring small variations in acceleration due to gravity, there remains uncertainty as to what gravity is. In the first edition of the *Encyclopedia Britannica,* published in 1771, the entry is one line: "Gravity, see Mechanics." Under Mechanics, there is a section labeled "acceleration of gravity," which starts, "gravity is that power by which distant bodies tend towards one another." By the fifteenth edition (1975, 1992 printing), gravitation is given its own section of nine pages, and gravitation is summarized as "a universal force of attraction acting between all matter" and which "is by far the weakest known force in nature. . . ." The concept of superstrings (having lengths of the order of Planck's length, 10^{-33} cm) shows promise of unifying the four forces cited in the introduction. These superstrings vibrate in different curled-up patterns in six dimensions of space (as Calabi-Yau manifolds) that are interpreted to exist at ultra small scale within our normally perceived four-dimensional space-time universe. Assigning a thickness (a two-dimensionality) to the superstrings brings our universe to having 11 dimensions of space-time. Also, gravitational "black holes" appear to be defined only by the same characteristics (mass, charge, and spin) as elementary particles [*Greene*, 1999; *Gibbons*, 2000].

Sets of spherical harmonic coefficients are used for defining the distribution of anomalies on a sphere. For a planet's gravity potential field they attempt, in a least mean squares sense, to best represent the spatial and magnitude variations represented in the data used to calculate the coefficients. These coefficients are analogous to the coefficients of Fourier transforms for data along lines, or on two-dimensional surfaces in a flat world. The equivalent wavelength λ for each harmonic degree is $2\pi R/n$: the planet's circumference divided by the harmonic degree number. Hence, for the Earth, with a circumference of about 40,000 km, the equivalent wavelength for degree 2 is 20,000 km, and individual positive or negative portions have individual widths of 10,000 km. Higher degrees obviously then represent shorter wavelengths. As higher spatial resolution data come available, solutions are extended to higher degree. The order coefficients for each degree provide information on anomaly pattern and magnitude representations along complementary cross sections of the planet. Power spectra for spherical harmonic coefficient sets for three planets (see Figure 2) show strong red spectra for both Earth and Mars, but the spectra for Venus has but a small range. To harmonic degree 10, the power spectra for Earth extends over 8 orders of magnitude, Mars extends over 5 orders of magnitude, and Venus extends over only 2 orders of magnitude. The patterns of power spectra summarize the global characteristics of a planet's potential field but provide little clue as to why the spectra differ. *O'Keefe and Kaula* [1963] noted that the Earth's power spectrum adhered approximately to a simple power law, which *Lambeck* [1976] and *Kaula* [1967] explained by a random distribution of density anomalies. These and other studies, however, reveal a nonrandom distribution of major Earth mass anomalies. When we began to investigate the possible causes of the Earth's geoid anomalies about 2 decades ago, the geodesy community insisted that one must deal only with the spectra and not analyze individual degree contributions. Now dealing with harmonic subsets has become common.

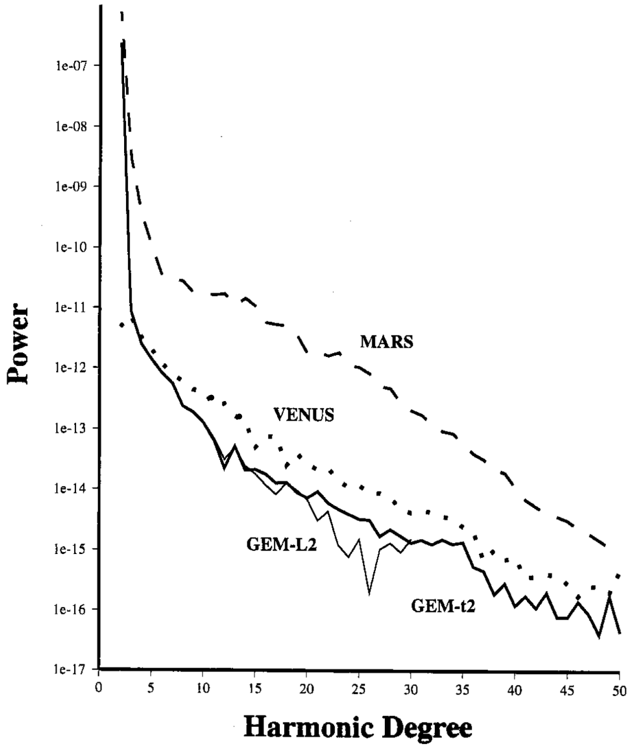

Figure 2. Power spectra for Earth, Venus, and Mars from sets of spherical harmonic coefficients. Earth (solid line) is from GEM-L2 [*Lerch et al.*, 1982] and GEM-t2 [*Marsh et al.*, 1990], Venus (dotted line) is from *Nerem et al.* [1993], and Mars (dashed line) is from *Smith et al.* [1993]. If the horizontal harmonic degree axis were plotted as a log scale, then the spectra would be nearly straight lines.

Gravity anomalies (which vary as inverse distance squared to mass anomaly sources (Newton's law)) can be integrated to estimate an equipotential surface (which varies only as inverse distance to mass anomaly sources), as in Plate 1. Gravitational equipotential values are scaled to equipotential elevation values via the formula of Bruns by dividing potential values by the mean surface gravity value (980.0 Gals, where Gal, for Galileo, is 1.0 cm s^{-2}). The ocean surface represents a gravity equipotential surface, called the geoid (wind, waves, and tides cause only minor local irregularities in the level of the sea). In the past, attempts to estimate the equivalent continuation of the level of sea level beneath continents had been subject to uncertainties due to unknown densities between the geoid and the free surface. However, with the advent of Earth-orbiting satellites the situation changed dramatically. Satellite data are now used to compute spherical harmonic coefficients C_{nm} and S_{nm}, which best represent the global variations. The spherical harmonic coefficients can then be used in the following equations to calculate geoid, or gravity (or even vertical gravity gradient), anomaly values at any selected latitude, longitude, and height locations:

$$\text{Geoid } N(\phi, \theta) = \frac{GM}{R}\frac{1}{g_0}\sum_{n=2}^{\infty}\sum_{m=0}^{n}\left(\frac{a_e}{R}\right)^n \cdot [C_{nm}\cos m\theta + S_{nm}\sin m\theta]P_{nm}(\sin\phi) \qquad (4)$$

$$\text{Gravity } g(\phi, \theta)m = \frac{GM}{R}\frac{1}{R}\sum_{n=2}^{\infty}\sum_{m=0}^{n}(n-1)\left(\frac{a_e}{R}\right)^n$$

$$\cdot\cdot[C_{nm}\cos m\theta + S_{nm}\sin m\theta]P_{nm}(\sin\phi), \quad (5)$$

where M is the mass of the Earth, R is the radius at location of the calculation, a_e is its equatorial radius, and g_0 is normal gravity, 980 cm s^{-2}. The arguments ϕ and θ are the geocentric latitude and longitude, respectively, at the location of the calculation. C_{nm} and S_{nm} are the fully normalized spherical harmonic coefficients of degree n and order m, referenced to an ellipsoid Earth. P_{nm} are the Legendre associated polynomials.

Global gravity potential fields are represented by sets of spherical harmonic coefficients. To better understand the principal geoid anomalies, the author [*Bowin*, 1994, 1998] prepared cumulative contribution curves (CCC) at the center locations of the Earth's 10 major geoid anomalies (Figure 3, top row). Such CCC curves reveal how the individual harmonic degrees sum at the center location to form an anomaly's magnitude. When first made, it was unknown to what extent values at some degrees would cancel contributions from other degrees. In fact, for most major geoid anomalies, the degree contributions sum rather consistently. Note that for greater than harmonic degree 10, the Earth's geoid values show very little change with additional higher-degree contributions. Note also that the two greatest positive and negative geoid anomalies have large contributions from degrees 2 and 3, followed by only small contributions from the individual degrees 4–10. A few other geoid features reveal a similar distinction in magnitude between contributions from degrees 2 and 3 and those of degree 4 and above. This is easily noted in Figure 4, as well as is the convergence to very small geoid degree contributions above degree 10. Scatterplots from a global gridded geoid data set demonstrate this magnitude distinction in another way (Figure 6a). Note that the degree 2–3 contribution dominates the 2–10 geoid field by contributing about 70% of the 2–10 values. The 4–10 geoid contributions are significantly less than those of the 2–3 packet, and the geoid contributions from degree 11 to point values (the residual geoid contributions remaining after subtraction of a regional degree 2–10 geoid) are very small.

The long-wavelength gravity anomalies, however, show subdued magnitudes relative to geoid anomalies. Whereas the envelopes of the geoid CCC are concave toward zero with increasing degree, the gravity CCC (Figure 3, top row) shows increasing free-air anomaly values for higher degrees. This same contrast is also reflected in the gravity scatterplots (Figure 5b). There the degree 2–3 gravity contributions are smallest and the 4–10 contributions are greater than those of degree 2–3, but the residual gravity contributions are even greater than those of the total regional 2–10 field. The actual range of gravity residual free-air anomalies is even larger than that represented in Figures 3 and 5. If the anomalies of island arcs and their adjacent deep-sea trenches would be better represented in these data sets, the range of the residual gravity anomalies would be from about −400 to +400 mGal (Figure 5). This contrast between geoid ($1/d$) and gravity ($1/d^2$) fields is a first indication that the greatest mass anomalies lie deep within the Earth. The CCC diagrams for Venus and Mars in Figure 3, conversely, suggest shallow sources for their major mass anomalies [*Bowin*, 1998], since their geoid anomalies coincide with surface topography.

Although gravity and geoid anomalies are only responsive to mass variations and their three-dimensional distributions, one cannot mathematically invert the global Earth geoid field to determine the interior distribution of the causative mass anomalies. This is because each individual mass body within the Earth contributes to the coefficients of every spherical harmonic degree, and thus determination of the Earth's internal mass anomaly structure has been considered to be essentially unresolvable from gravity data.

Maximum geoid anomalies lie in the range of ±100 m, and the maximum free-air gravity anomalies lie within the range ±400 mGal. However, the locations of their maxima show no consistent relation to each other. The greatest magnitude geoid anomaly (−103 m) lies in the Indian Ocean south of the southern tip of India (hereinafter referred to as the Sri Lanka (SL) anomaly), and the greatest positive geoid anomaly (+80 m) occurs near New Guinea (NG) (Plate 1). The greatest negative free-air gravity anomalies lie over the deep-sea trenches associated with subduction zones seaward of island arcs. The volcanic island arcs themselves are the sites of the greatest positive free-air gravity anomalies on the Earth. Together, the trench/arc gravity anomalies make a pair of complimentary anomalies whose crests and troughs lie within a few hundred kilometers of each other [*Bowin*, 1991, Figures 5 and 6]. Because of the short wavelengths of island arcs and their trenches, and the trench/arc close spatial association, their positive and negative gravity anomalies of these surface structures essentially cancel each other and yield no significant long-wavelength contribution to the gravity anomaly spectrum. The global pattern of geoid anomalies (Plate 1, degrees 2–50) was a surprise, as no consistent correlation with topography, plate tectonic patterns, or magnetic field is discernable.

The CCC (Figure 3) and scatter (Figure 5) diagrams suggest that degrees 2–10 suffice to define the regional geoid field of the Earth and that the regional field is principally composed of two different sources. The first source (deep) is mostly responsible for the large energy of degrees 2 and 3, and the second (shallower) source is principally responsible for the remaining degree 4–10 contributions. The degree 2–10, 4–10, and 2–3 maps shown in Plate 2 are compatible with that two-source interpretation. Much smaller crustal mass anomalies in the outer 100 km of the Earth contribute to the large residual gravity anomalies (Figure 6). The low magni-

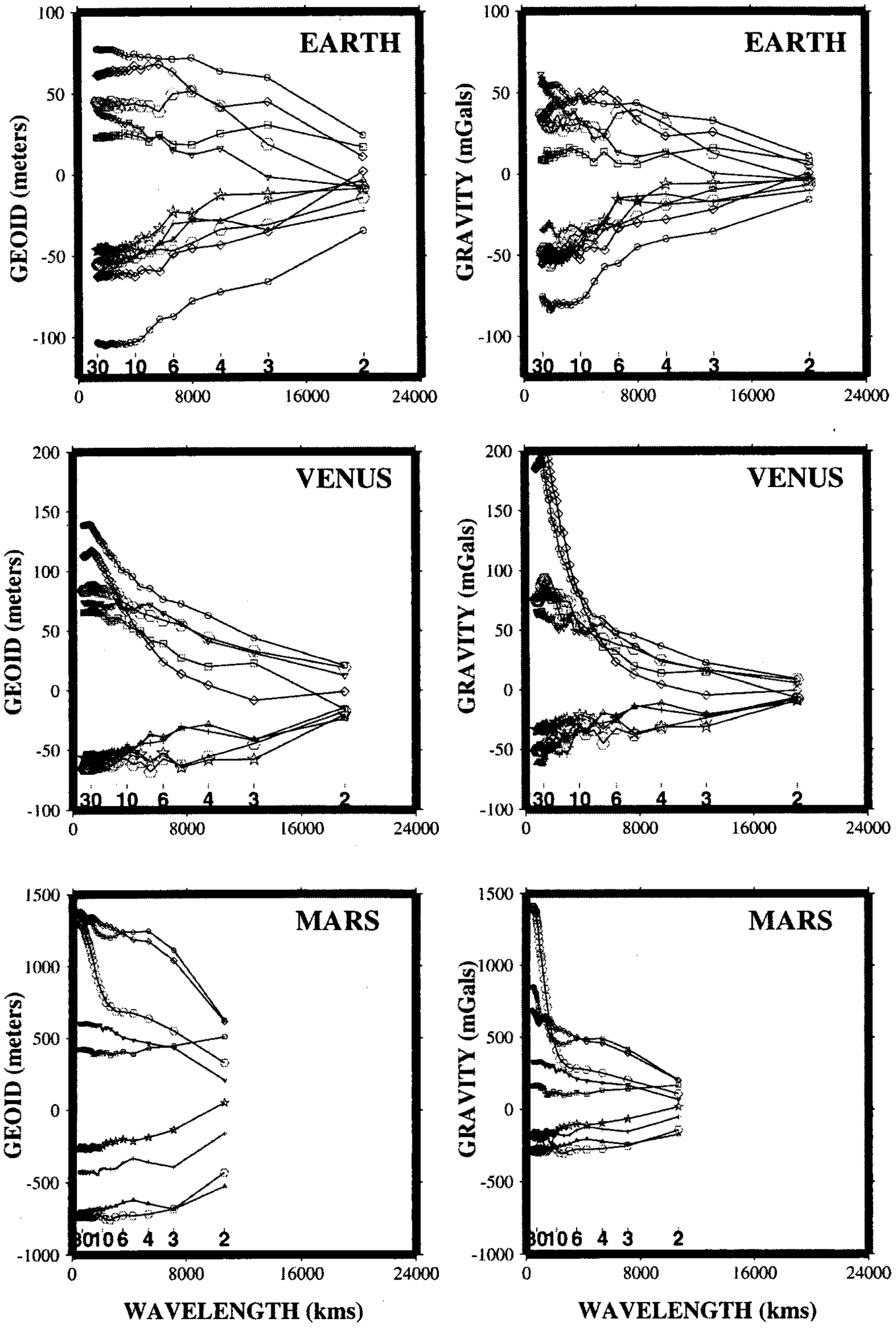

Figure 3. (a) Geoid and (b) gravity cumulative contribution curves for the major geoid anomaly features of Earth, Venus, and Mars computed at the center locations for each planet's major geoid anomaly features. The Earth curves were computed from GEM-t2 coefficients, referenced with reciprocal flattening of 298.257 (actual Earth flattening). Four positive anomalies are New Guinea (circles), Iceland (diamonds), Crozet (hexagons), and South America (inverted triangles). Six negative anomalies are Indian Ocean (Sri Lanka) (circles), west of lower California (plus signs), central Asia (hexagons), and south of New Zealand (stars). Venus values are from GVM-1 coefficients, and Mars values are from GMM-1 coefficients. The smaller wavelength values for Mars reflect its smaller size. Zonal coefficients for degrees 2, 4, and 6 were set to zero for Earth and Mars so that the equatorial bulge (mostly due to rotation) would not obscure the geoid pattern and for Mars would not obscure the pattern that corresponds with topography. Venus rotates so slowly it is spherical, not oblate. Reprinted from *Bowin* [1998] with permission.

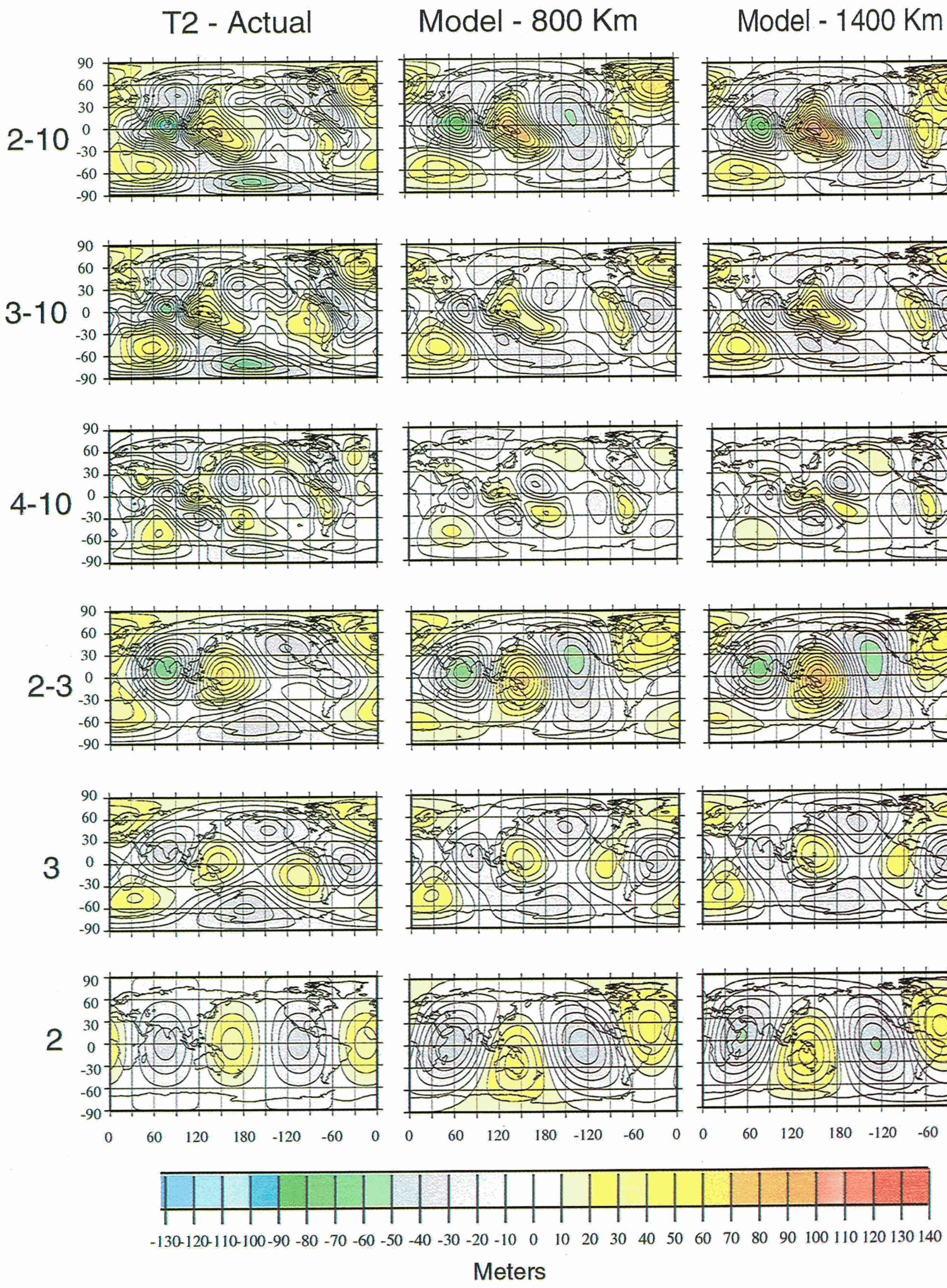

Plate 2. Global geoid anomaly maps for spherical harmonic degree ranges. Left column is for GEM-t2 spherical harmonic coefficients [*Marsh et al.*, 1990] with actual inverse flattening (298.257). Center column is the 800-km Earth mass anomaly model with four core-mantle boundary (CMB) point masses. Right column is the 1400-km Earth mass anomaly model with the same four CMB point masses.

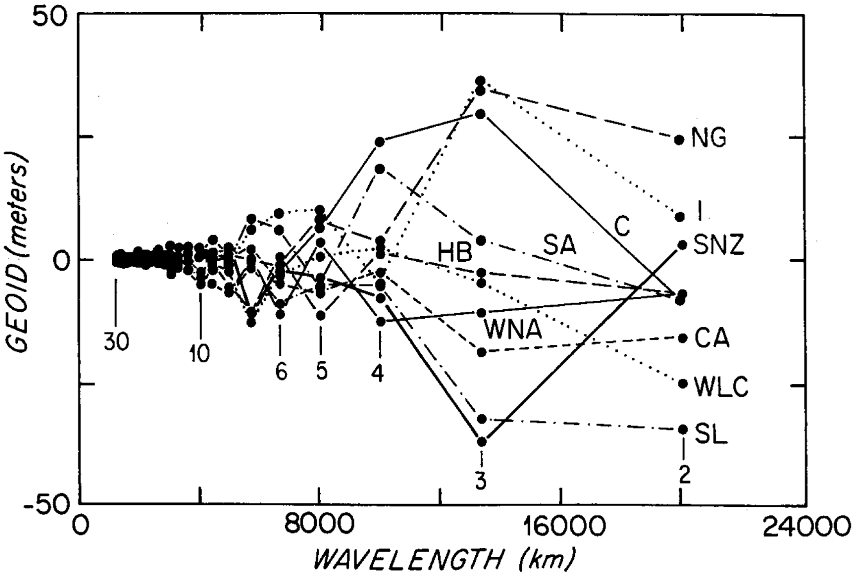

Figure 4. Magnitudes of individual harmonic degree contributions for the Earth's 10 major geoid anomalies. Values are computed from GEM-9 coefficients, referenced with reciprocal flattening of 298.257 (actual Earth flattening). Four positive anomalies are New Guinea (NG), Iceland (I), Crozet (C), and South America (SA). Six negative anomalies are Indian Ocean (Sri Lanka) (SL), west of lower California (WLC), central Asia (CA), south of New Zealand (SNZ). Reprinted from *Bowin* [1985] with permission.

tude of the gravity degree 2–3 anomalies (in contrast with the strong geoid degree 2–3 anomalies) suggests that the degree 2–3 source is very deep in the Earth. Furthermore, the degree 4–10 pattern defines bands of positive geoid anomalies that correlate with sites of plate tectonic subduction, adding further credence to the idea of separating the regional geoid into two main parts.

The fact that bands of positive anomalies in the degree 4–10 geoid pattern match well with locations of subduction zones, whereas the greater anomalies of the 2–10 geoid do not, was puzzling. Dynamic topography solutions attempt to explain this apparent dichotomy as resulting from a single process. That process comprises positive mass anomalies of subducted slabs sinking in a viscous convecting mantle. That sinking produces compensating boundary deflections (surface, 670 km, and core-mantle boundary (CMB)), whose degree 2 and 3 contributions overwhelm the smaller degree 4–10 contributions from the subducted slabs to yield the puzzling geoid pattern seen in Plate 1. However, a more simple explanation can account for this evidence: Very large mass anomalies lie deep in the Earth, and only much smaller mass anomalies occur at shallower levels. The principal distinction is whether one is willing to accept the possibility that processes within the Earth's core may generate the Earth's deep largest mass anomalies. Such mass anomalies presumably would result from CMB topography induced at this great density interface. The dynamic topography proponents, because of the fluid nature of the core, consider that processes within the mantle must produce any perturbations of the CMB, if they exist. However, if CMB perturbations do not exist, then the dynamic topography solutions have lost their mechanism for producing degree 2 and 3 contributions that might overwhelm the 4–10 geoid pattern. Also, proponents of the alternate explanation would have to say that the Earth's geoid would not look the way it does.

Global images of the Earth's regional geoid, referenced to the actual geometric figure of the Earth (Plate 2, left column) and to the hydrostatic figure (Plate 3, left column), computed from spherical harmonic coefficients for the Goddard Earth Model GEM-t2 [*Marsh et al.*, 1990] are shown for six different packets of harmonic degrees. These degree packets (2–10, 3–10, 4–10, 2–3, 3, and 2) help show the composition of the anomalous geoid field. Similar plots for degrees 2–10 are given by *Bowin* [1991, Figures 2 and 4] for GEM-L2 coefficients. Degree zero is a mean value for the entire Earth, and degree 1 provides a measure of any displacement of the center of mass from the center of figure. *O'Keefe and Kaula* [1963] discuss why it is desirable to use the hydrostatic reference figure for tectonic analyses while acknowledging that the discrepancy between the actual (geometric) and equilibrium (dynamic) figures could be considered as a lag of 10^7 years in adjustment to the slowing of the Earth's rotation [*Munk and MacDonald*, 1960]. That statement was used herein to justify modifying the C_{20} coefficients for our spherical Earth 800- and 1400-km models to simulate hydrostatic anomalies in Plate 3. The hydrostatic flattening figure (1/299.638) has been computed by *Nakiboglu* [1982].

The previously shown figures and plates are for geoid and gravity data referenced to the Earth's figure with an

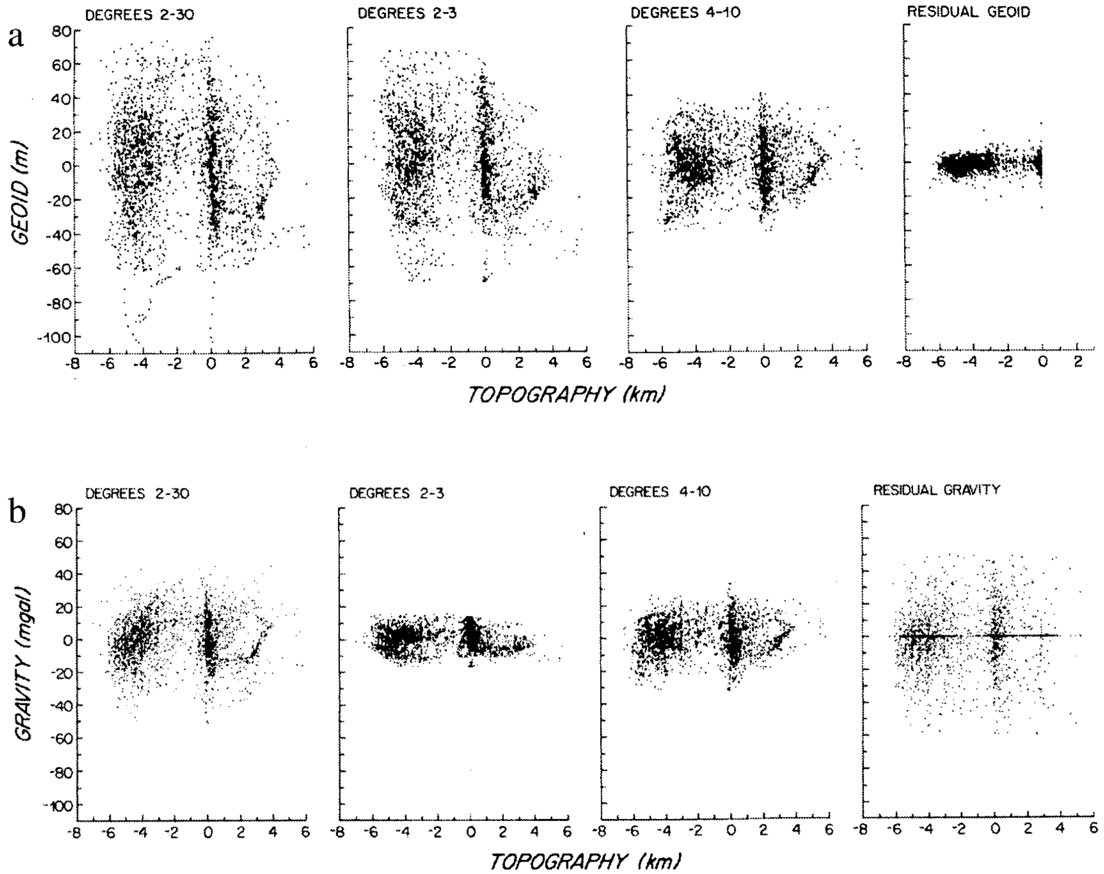

Figure 5. (a) Geoid anomaly versus topographical elevation. All geoid anomaly values are referenced with reciprocal flattening of 298.257 (actual Earth flattening). The harmonic degree geoid data are from the gridded global data set used to prepare geoid anomaly maps from GEM-L2 coefficients published by *Bowin* [1991, Figure 1]. The residual geoid global data are from *Bowin* [1991, Figure 5], but only every hundredth point is plotted. (b) Gravity anomaly versus topographic elevation. The harmonic degree gravity data are also from GEM-L2 coefficients referenced with reciprocal flattening of 298.257. The residual gravity global data are from *Bowin* [1991, Figure 6], but only every hundredth point is plotted. Reprinted from *Bowin* [1991] with permission.

actual geometric flattening of (f^{-1} = 1/298.3). These anomalies are observable facts and provide an objective view of the Earth's mass anomalies. The hydrostatic figure, on the other hand, is not directly observable and must be computed from theoretical considerations. The hydrostatic equilibrium figure attempts to separate (and identify) the mass anomalies that actively stress the Earth from those that are now in equilibrium. There is no independent way to distinguish nonhydrostatic stress completely from hydrostatic stress. *Goldreich and Toomre* [1969] proposed that the Earth's larger equatorial radius is not due to a "fossil bulge," which would require mantle viscosities of about 10^{24} Pa s^{-1}. They concluded that the "nonhydrostatic bulge" is not a spheroid and that the nonhydrostatic Earth should be considered as a collection of more or less random density inhomogeneities. From that it follows that polar wander will adjust the position of the rotation axis of the Earth until it coincides with the axis of maximum moment of inertia of any nonhydrostatic mass distribution (such as that due to mantle convection or subduction). *Ricard et al.* [1993a] find that with a viscoelastic relaxation model in which the mantle has a viscosity of 10^{21} Pa s^{-1}, the excess flattening due to a delayed response of the Earth to tidal deceleration is only about 20 cm; whereas the nonhydrostatic flattening, due to the fact that polar wander adjusts the rotation axis on geological timescales in such a way that excess mass becomes situated around the equator, is determined to be about 100 m, 500 times larger than the tidal deceleration contribution for these model assumptions. If these conditions are the case, they would negate the *O'Keefe and Kaula* [1963] rationale for our simply modifying the C_{20} coefficient used in Plate 3 to display a simulated hydrostatic flattening from our spherical Earth mass model. However, *Denis et al.* [1997] argue that the hydrostatic value that is commonly referred to as the hydrostatic flattening is merely a conventional value computed from the following relation, derived from the first-order Clairaut-Radau theory [*Moritz*, 1990]:

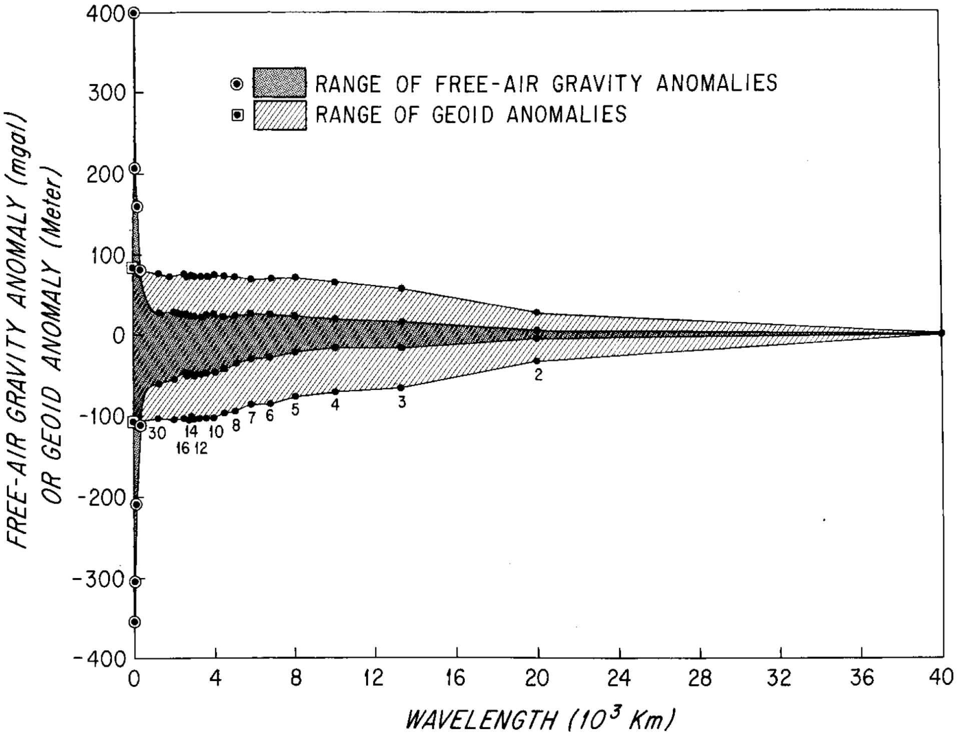

Figure 6. Comparison of the ranges of free-air gravity anomalies and geoid anomalies as a function of anomaly wavelength. The numbered dots are computed from spherical harmonic coefficients (GEM-9) [*Lerch et al.*, 1979]. The circled dots at zero wavelength (−380 and +40 mGal) show the range of point gravity measurements from a representative sample of global observations (Figure 5). The three other circled dots, not quite at zero wavelength, indicate the range of 20′ × 20′, 1° × 1°, and 2° × 2° averaged gravity measurements in the Caribbean region [*Bowin*, 1976]. The squared dot geoid values at zero wavelength are derived from map of *Rapp* [1979]. Note that the great increase in the range of gravity anomalies only occurs at very short wavelengths. Reprinted from *Bowin* [1983] with permission.

$$f^{-1} = \frac{2}{5m}\left[\left(\frac{5}{2} - \frac{15}{4}\frac{J_2}{H}\right)^2 + 1\right], \qquad (6)$$

where f^{-1} is inverse flattening, J_2 is the kinetic shape factor, m is the geodynamical constant (the ratio of centrifugal to gravity acceleration at the equator, 0.33344), and H is the processional constant. Later, we will also refer to y (an inertia coefficient taken as = J_2/H). Putting observed values into (6), the value $f^{-1} \approx 299.9$. Since the early 1960s this has been considered to be the actual hydrostatic flattening of the Earth. It differs significantly from the observed value $f^{-1} \approx 298.3$ and from the value obtained by inserting the observed values of m and J_2 into Clairaut's formula (equation (7), below), i.e., $f^{-1} \approx 298.6$:

$$f = \tfrac{1}{2}(m + 3J_2) \qquad (7)$$

and y computed from

$$y = \frac{2}{3} - \frac{4}{15}\sqrt{\frac{5m}{2f}} - 1. \qquad (8)$$

It is (7) that *Denis et al.* [1997] consider to be most appropriate, because it is fully consistent with hydrostatic theory. Equation (6) is, in principle, only consistent with hydrostatic theory if hydrostatic equilibrium actually occurs. However, the Earth is not in hydrostatic equilibrium.

The inertia coefficient ($y = J_2/H = 0.3308 \approx 0.331$), consistent with $f^{-1} \approx 299.9$, is used to constrain all modern Earth models. It leads to f, J_2, and H model values that are incompatible with their observed counterparts and overestimates the actual departure of the real Earth from hydrostatic equilibrium. *Denis et al.* [1997] note that perfect agreement is impossible because the Earth is definitely not in hydrostatic equilibrium and that there is no independent means of separating nonhydrostatic stress from hydrostatic stress. In particular, they emphasize that one cannot simultaneously choose f and y and that this fundamental fact has been ignored by members of the Standard Earth Model Committee of the International Union of Geodesy and Geophysics. *Denis et al.* [1997; 1998] conclude that the use of an inertia coefficient $y \approx 0.332$ can bring free core nutation and the spectral splitting of free mode multiplets into closer agreement with a consistent hydrostatic theory than previously assumed. The 0.332 value also significantly alters the density structure of the core, notably making the density jump at the inner core boundary

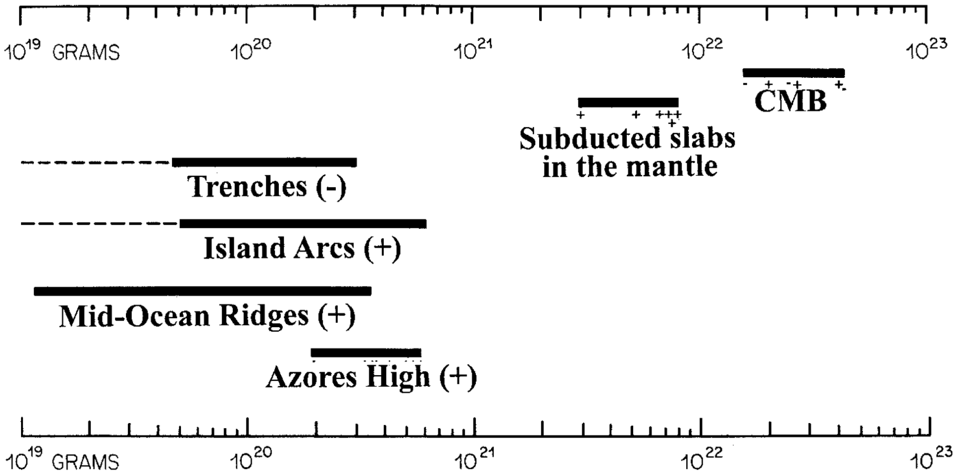

Figure 7. Initial estimates of the magnitudes of Earth mass anomalies. Estimates are calculated from ratios of gravity anomaly divided by geoid anomaly values at anomaly centers (see text). Reprinted from *Bowin* [1994] with permission.

smaller than that assumed in the preliminary reference Earth model (PREM) [*Dziewonski and Anderson*, 1981]. Thus for now we leave Plate 3 as an example that our spherical Earth models might possibly be made to match an Earth hydrostatic geoid, particularly one with an inverse flattening value of 298.6.

Because all masses within the Earth contribute to all harmonic degrees, it is impossible to invert geoid anomalies in order to determine the causative anomalous masses. Thus the anomalous mass distribution within the Earth has remained unsolved. Some estimates have been made, however. One procedure involves ratios of gravity integrals and derivatives [*Bowin et al.*, 1986; *Bowin*, 1983, 1986, 1998] utilizing point-mass models as a useful start. This is because they indicate the maximum possible depth for a source of an anomaly (assuming it has a single positive or negative mass cause). At a site directly over the center of a point mass the geoid anomaly is

$$N = \frac{V}{g_0} = \frac{GM}{g_0 z}, \tag{9}$$

where V is the disturbing potential, g_0 is normal gravity (9.8 m s^{-2}), G is the gravitational constant, M is the anomalous mass, and z is the depth of the point mass. The vertical component of gravity g due to the same point mass is

$$g = \frac{GM}{z^2}. \tag{10}$$

The ratio of the gravity anomaly to the geoid anomaly directly above the point mass at depth z is then

$$\frac{g}{N} = \frac{g_0}{z}. \tag{11}$$

Conversely, the depth can be determined by

$$z = \frac{g_0}{g/N}. \tag{12}$$

Then, of course, reentering this value for z into either or both (9) and (10) can provide an initial estimate of the causative mass. Application of this procedure to Earth gravity and geoid anomalies provided the estimates shown in Figure 7, which suggests that deep masses (perhaps 100 times greater than that of the mass anomalies of principal surface structures) are responsible for the largest geoid anomalies. A mass value of 1.0×10^{21} kg appears to divide the deep source anomalies producing the Earth's regional geoid field (degrees 2–10) from those of the residual anomalies (degrees >10) of Figure 5. Note also that low-magnitude geoid and gravity anomalies do not necessarily relate to low mass values. Mid-ocean ridges, because of their broad extent, locally attain mass anomaly magnitudes comparable to those of deep-sea trenches and island arcs, which have the greatest gravity anomalies. This illustration gave further support to the view of Earth structure emerging from Figures 3, 4, and 5. In hindsight, the author now sees he was applying perturbation theory in attempting to resolve Earth structure. The deepest mass anomalies dominate the contributions to the Earth's geoid. Thus their source could be isolated and explained, as a first approximation, by topography at the CMB. Together with the smaller mantle subduction zone positive mass anomalies, they completely accounted for the regional geoid field.

Figure 8 shows equivalent point-mass depths calculated from gravity over geoid (g/N) ratios for individual harmonic degree contributions. Note that only degrees 2 and 3 have equivalent point-mass depths deeper than the CMB, and thus if there are mass anomalies at the CMB, their harmonic degree contributions should be greatest for these two degrees. However, great, broad,

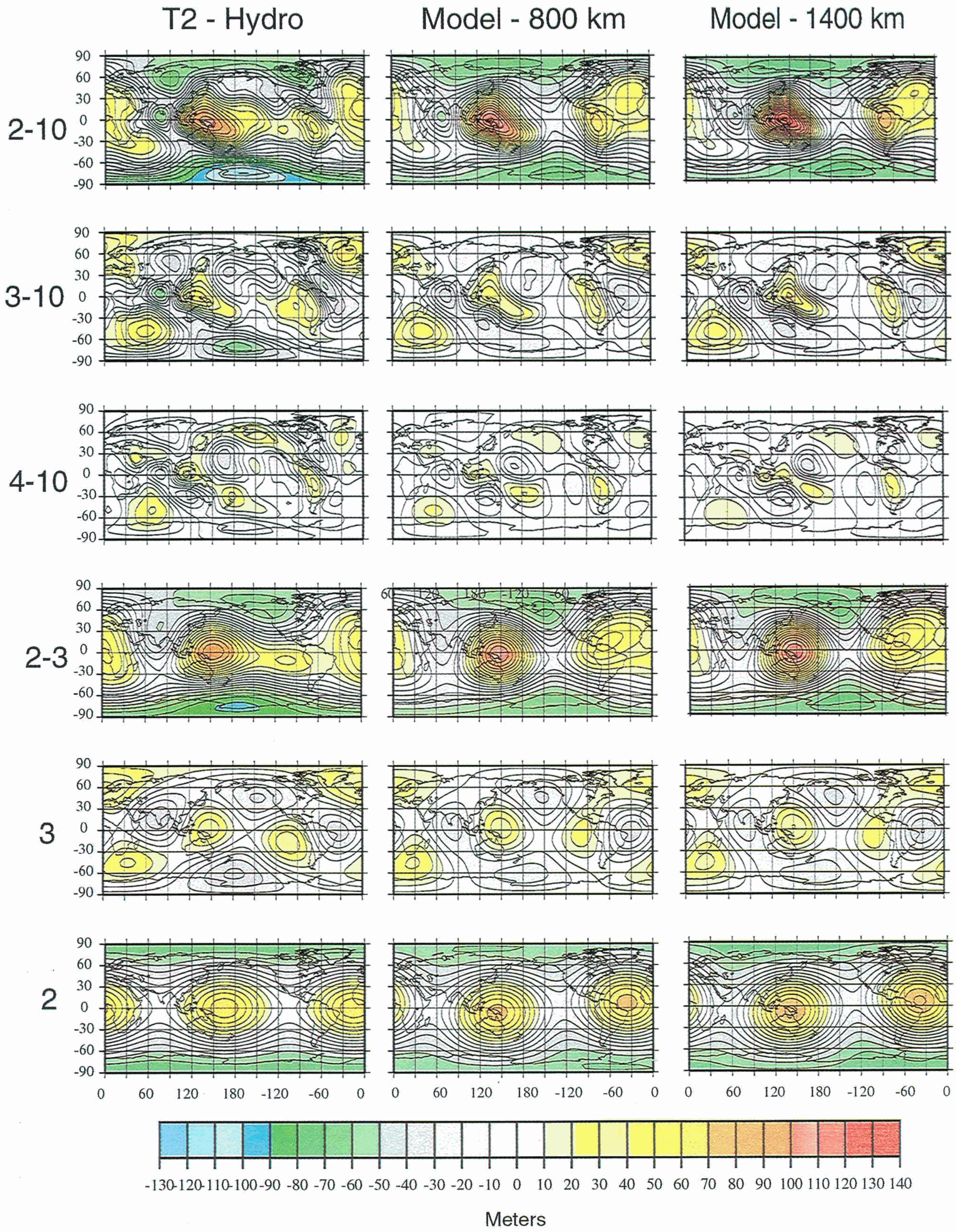

Plate 3. Global geoid anomaly maps for spherical harmonic degree ranges. Left column is for GEM-t2 spherical harmonic coefficients [*Marsh et al.*, 1990] with hydrostatic flattening (299.638). Center column is the 800-km Earth mass anomaly model. Right column is the 1400-km Earth mass anomaly model.

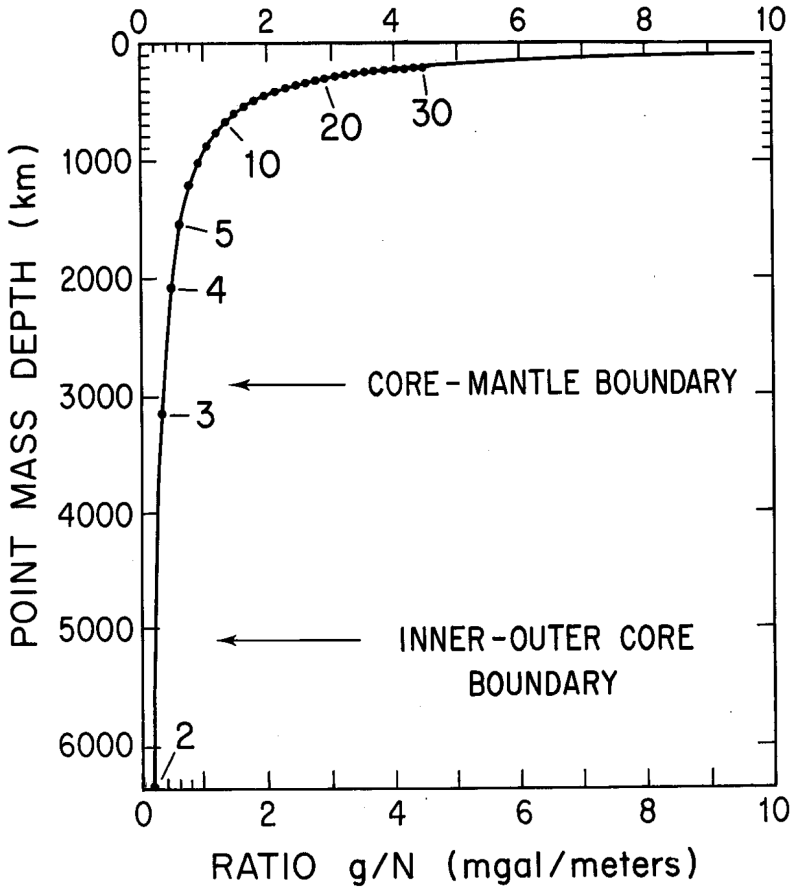

Figure 8. Ratio of gravity to geoid anomalies as a function of depth to a point-mass source. Dots along the curve indicate the ratio for individual harmonic degree contributions (labeled as to degree). The depth associated with each harmonic degree is that of a point mass having the same gravity to geoid ratio. Reprinted from *Bowin* [1983] with permission.

and shallow mass anomalies, of course, would also contribute significantly to harmonic degrees 2 and 3, such as the case of Mars (Figure 3). It was also concluded that such great deep mass anomalies in the Earth most likely result from topography of the CMB because of the 4.34 g cm^{-3} density change across that boundary between lower mantle silicates and nickel-iron of the fluid metallic outer core. This CMB density contrast value is obtained from the PREM density model for the Earth derived to satisfy seismological travel time data [*Dziewonski and Anderson*, 1981]. Figure 9 shows the PREM density profile and percentages of total variance of several depth ranges for both geoid and gravity anomalies.

Another estimate of internal mass distribution utilized statistical forward models [*Jackson et al.*, 1991]. Jackson et al. concluded that "monopolar" mass anomalies in the lower mantle, but not associated with CMB topography, must generate the Earth's strong low-degree geoid anomalies. Their conclusion follows from a view that mantle convection in which there is a moving distribution of mantle mass anomaly would be partially compensated by a deformable CMB, and hence the surface geoid anomaly would be diminished. Neither the nature nor the origin of the monopolar masses was provided. Mass anomaly estimates have also been made indirectly by using dynamic mantle convection models [*Ricard et al.*, 1993b; *Lithgow-Bertelloni and Richards*, 1998]. These are discussed below.

4. MASS ANOMALY STRUCTURE OF THE EARTH

The strongest evidence indicating that dynamic topography solutions may not play the dominant role in contributing to the Earth's geoid field is probably the South American Andes regional geoid anomaly. It is the Earth's fourth greatest positive geoid anomaly. The distinction between the broad regional geoid anomaly and the local geoid high associated with the high topography of the Altiplano-Puna segment of the Andes is readily observable in Figure 10, reproduced from *Froidevaux and Isacks* [1984, Figure 3]. In the dynamic topography solutions [*Ricard et al.*, 1993b, Figure 14; *Lithgow-Bertelloni and Richards*, 1998] a surface depression of some 1500 m is inferred to exist above the South American subduction zone. A larger depression of the CMB would also exist at depth, with both depressions (equivalent to

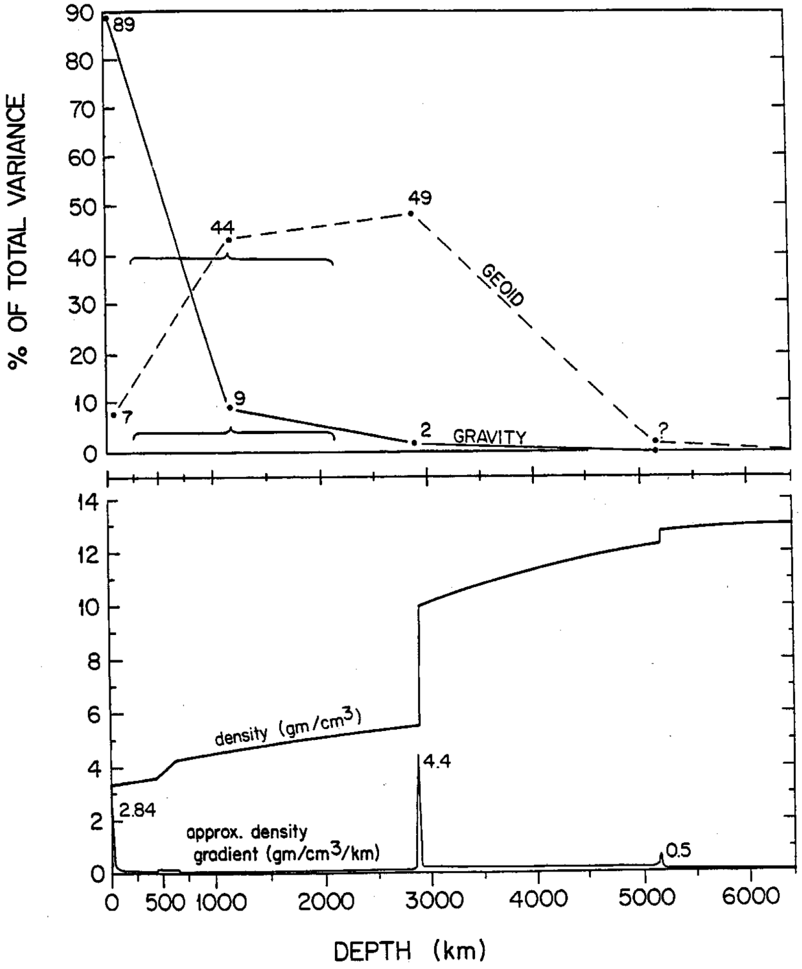

Figure 9. (bottom) Density and density gradient and (top) relative contributions to gravity and geoid anomalies. The large change in density at 2900-km depth is at the CMB. Data are from *Bullen* [1975], *Jordan* [1978], and the author. Percentage of total variance of geoid and gravity values are for (from right to left) degrees 2–3, 4–10, and residual anomalies of degrees greater than 10. Reprinted from *Bowin* [1983] with permission.

negative masses) providing compensation for the positive mass in the intervening South American subduction zone. Hence three different masses at three different depths are invoked to produce the total regional geoid anomaly there. Our evidence below indicates that only a single positive mantle mass anomaly accounts for the South American regional geoid high.

CCC plots display how the maximum anomaly value for a planet's major geoid anomalies attain their maximum values (Figure 3) [*Bowin*, 1994, Figure 2]. In order to estimate an equivalent point-mass source depth from geoid or gravity data, where depth is only one of several contributors (e.g., depth, mass, and its three-dimensional configuration), some sort of normalization to reduce the number of variables is required. The normalization relation presently used is the percentage of the variable's value at harmonic degree 30. Degree 30 is chosen because for the Earth, the major geoid anomalies have only small contributions from harmonic degrees above 10 (Figures 3 and 4) [*Bowin*, 1991, Figure 9a] and because the coefficients of GEM-L2, t1, and t2 and other modern solutions remain well determined to degree 30 or higher.

Although the regional South American geoid high is likely attributable to a localized mass distribution (modeled by a point mass), we cannot directly insert a point mass to generate the harmonic coefficients, because it would generate degree 1 terms not present in the observed Earth harmonic coefficients. To overcome this difficulty, we put auxiliary point masses (one for even degrees and two for odd degrees) in symmetry with the main point mass to balance out degree 1 terms from each individually. These auxiliary points are the simplest representation of the environment of mass anomalies in which the main point mass finds itself. Since our goal is to study the geoid and gravity features right above the point mass, this auxiliary point method is adequate enough for our purpose. We placed the balanced sets at six different depths (100, 500, 1000, 2000, 2900, and 4000 km). Then CCC plots were made for a location directly

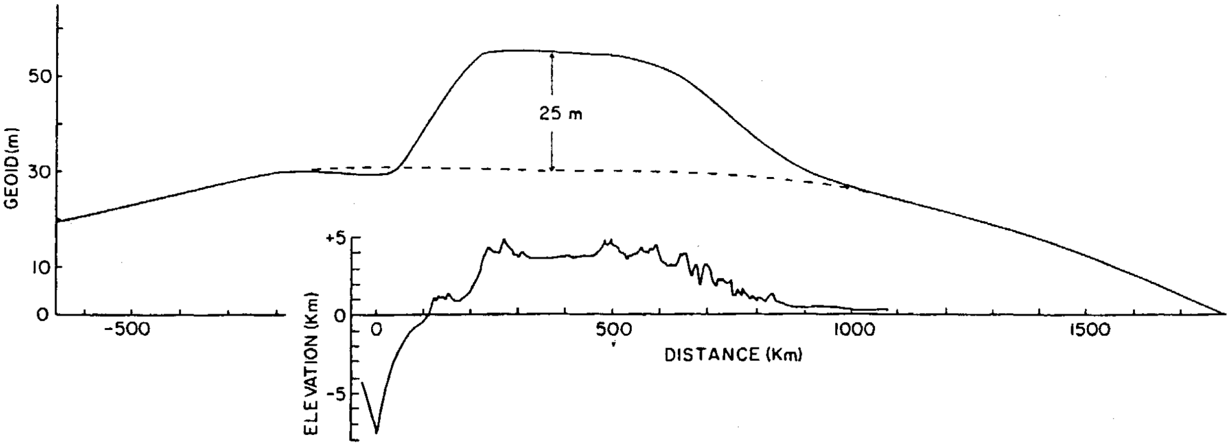

Figure 10. Geoid height and topography along an east-west profile around 20°S. The horizontal distance is measured relative to the oceanic trench axis. A distinct deflection in the geoid curve, $N = 25$ m, correlates with the high topography of the Altiplano-Puna and of the Eastern Cordillera. The dashed line is drawn in continuation of the broader regional maximum. Reprinted from *Froidevaux and Isacks* [1984] with permission.

above one of the positive point masses used in each model (Figures 11 and 12) [*Bowin*, 1994, Figure 4]. Sets of both odd and even numbers of point masses at each depth had to be used in order to get harmonic coefficients for both odd and even degrees. This is because for the odd number of positive point masses, the even harmonic degree coefficients equaled zero, and the opposite was true for the even number of point masses. Figure 11 shows geoid percentage CCC curves for each of the six model depths. Note that at each odd degree it would be possible to prepare an interpolator that could estimate an equivalent point-mass depth for any geoid percentage value. In Figure 12 (for even degrees) the geoid curve for 100-km depth forms a nearly straight line from degree 0 to degree 30, with, for example, a degree 2 value of about 7%. With increasing model depths the geoid percentage curves become increasingly convex upward, with, for example, the degree 2 value changing: 500 km (12%), 1000 km (20%), 2000 km (42%), 2900 km (57%), and 4000 km (77%). At 100-km depth the higher derivative curves (gravity, vertical gravity gradient, and vertical gradient of vertical gradient of gravity) form curves beneath the geoid curve increasingly concave upward. As the model depths increase, the first derivative gravity curve is closest to a straight line at 500-km depth, and the second vertical derivative vertical gravity gradient curve becomes closest to a straight line at 1000-km depth. By 2000-km depth all derivative curves are convex upward (Figure 12).

Spline functions (for a smooth interpolation) for each degree (and each derivative) were fit to the balanced model normalized percentage values. By then applying those spline functions to observed (or model) normalized percentage data, an estimate of an equivalent point-mass depth can be made at each and every harmonic degree between 2 and 29. The degree and consistency between these individual harmonic degree estimates, in turn, provide a measure of how closely the causative mass anomaly sources are to being equivalent to point masses at a single depth. Additional information on such degree of consistency is provided by the higher derivatives of the potential field ($N = 1/d$), that is, gravity ($g = 1/d^2$), the vertical gravity gradient ($y = 1/d^3$), and the vertical gradient of vertical gravity gradient ($v = 1/d^4$). It must be recognized here that the multiple curves of the percentage CCC plots do not represent independent information since all are derived from the same spherical harmonic coefficients. However, we also recognize that planetary spherical harmonic coefficients

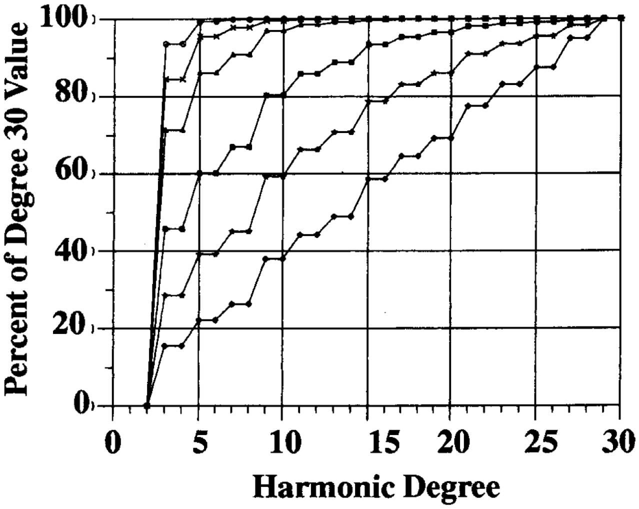

Figure 11. Set of geoid cumulative percent curves at a location directly above a positive model point mass. Curves are computed from spherical harmonic coefficients determined from balanced sets of point masses (three positive and three negative) at the label depths. Curves show summed contributions from degrees 2–30 for depths (top to bottom) 4000, 2900, 2000, 1000, 500, and 100 km.

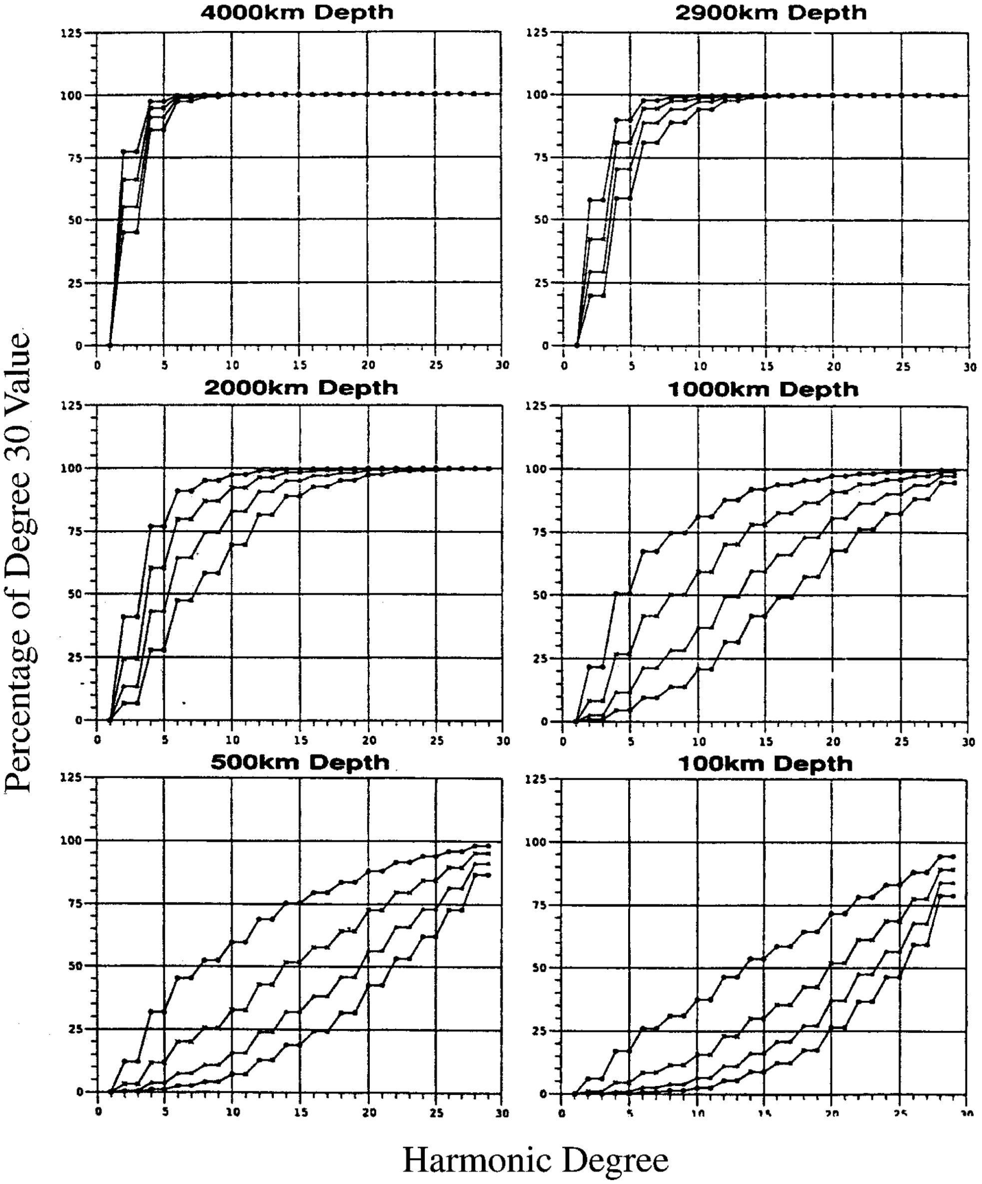

Figure 12. Sets of cumulative percent curves at a location directly above a positive model point mass. Curves are computed from spherical harmonic coefficients determined from balanced sets of point masses (two positive and two negative) at the label depths. In each set the curves (from top to bottom) are for geoid, gravity, vertical gravity gradient, and vertical gradient of the vertical gravity gradient anomalies. Reprinted from *Bowin* [1994] with permission.

are attempting to assimilate signals from a multiplicity of mass anomaly sources (shallow, deep, intermediate, compact, broad, elongate, etc.) and that different derivatives have modified responses from different source depths and configurations. Very deep sources will most profoundly influence the low harmonic degree geoid percentage values, whereas shallow compact sources will most profoundly influence the high-degree gradient of gradient harmonic percentage values.

The regional South American (SA) geoid high attains a hydrostatic anomaly value of 62.2 m at degree 30 from the summation of its individual degree contributions. Applying the above spline functions to the percentage CCC data for the hydrostatic SA geoid high produces the equivalent point-mass depth data shown in Figure 13. The SA percentage CCC plot (Figure 13) shows consistent equivalent point-mass depths of near 1200 km, not only for nearly all degrees for the geoid but also for all its derivatives. These results strongly suggest that the mass anomalies producing the broad regional SA geoid high (of up to degree 30) have basically a single equivalent point-mass depth in the mantle. Thus they do not result from a combination of sources at three distinctly different depths (surface, mantle, and CMB), as inferred by the dynamic topography models. The real mass anomalies, of course, must occur at depths shal-

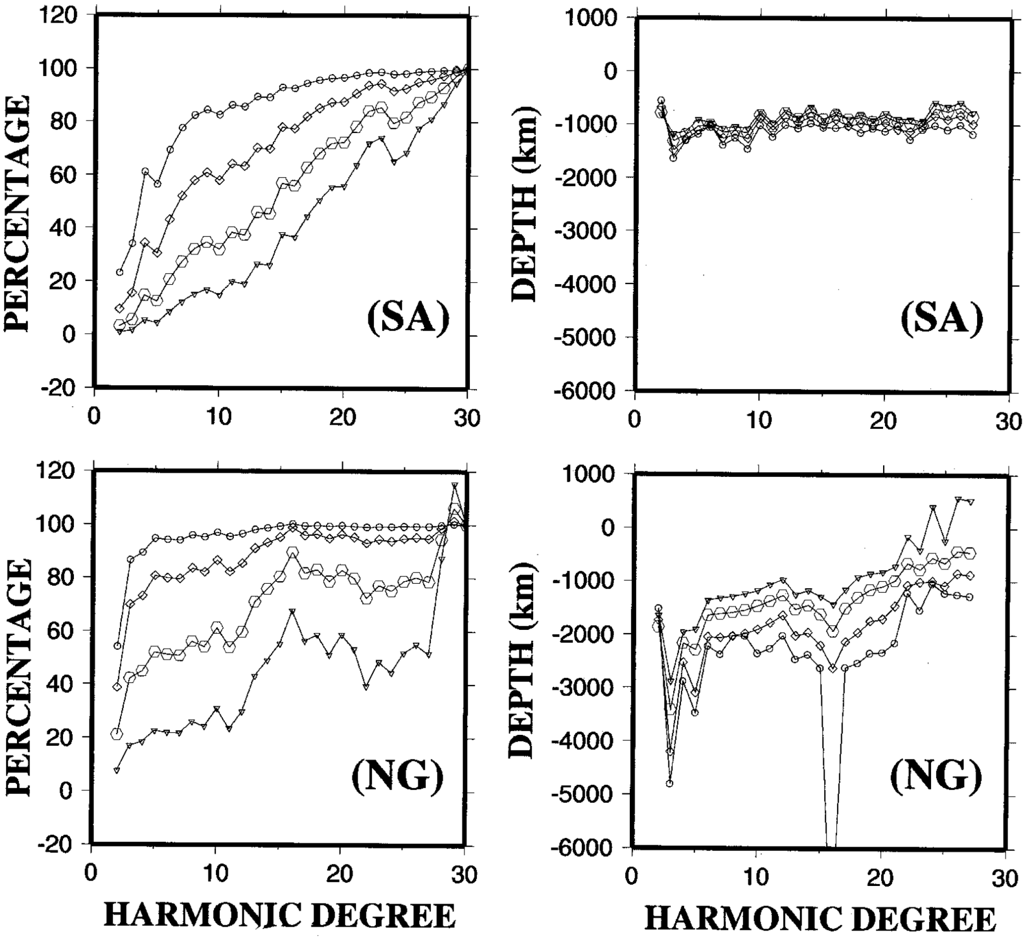

Figure 13. Percentage cumulative contribution curves (CCC), estimated equivalent point-mass depth curves, and estimated anomalous mass. Depths are estimated from the percentage CCC using spline function coefficients for each degree. Spline functions are from model sets of 2 and 3 balanced point masses at depths of 100, 500, 1000, 2900, and 4000 km. SA indicates South America GEM-t2 degree 2–10 geoid high, and NG indicates New Guinea GEM-t2 degree 2–10 geoid high.

lower than the equivalent point-mass depth. Balanced mass anomaly models having sources at three depths support that conclusion by showing a vertical separation among the geoid and its three vertical derivative curves.

The percentage CCC data for the hydrostatic New Guinea (NG) geoid high and the derived estimated equivalent point-mass depths are shown in Figure 13, bottom row. Figure 13 shows that 86.58% of that anomaly's degree 30 geoid value is reached at degree 3, indeed, a very high percentage. Note also the distinct vertical separation of the derivative curves (Figure 13, bottom row), indicating sources at multiple depths.

5. DYNAMIC TOPOGRAPHY

Dynamic topography studies incorporate the relationship between thermally driven flow in the Earth and geoid anomalies as outlined by *Pekeris* [1935]. He showed that flow produced by an internal driving density anomaly in a viscous Earth (e.g., subducted slabs with positive density anomalies) could induce deformations of surface and internal density boundaries. Boundary deformations, like subsidence of the Earth's surface above a subducting mass, and depression of the CMB beneath the subducting mass might produce negative compensating geoid contributions. These negative contributions would counteract the positive contribution from the subducting mass, thereby greatly modifying the simple positive geoid anomaly expected from a positive subducting mass in a rigid or elastic Earth. Indeed, interface deflections in response to a falling mass in a viscous environment are necessary for force equilibrium. Dynamic topography is a "snapshot theory"; it assumes that after millions of years of unspecified flow, the mass distribution has come to the current stage revealed by the seismic tomography and that the outer and internal boundaries must be in dynamic balance with the driving mass distribution. Can the magnitude of the negative mass compensating deflections, though, exceed that of the driving positive masses? *Richards and Hager* [1984] present an argument how this may be the case for flow in a mantle having uniform viscosity acting upon internal density boundaries.

The most detailed information regarding deep Earth structure has come from seismic tomography utilizing both *P* and *S* waves produced by earthquakes and nuclear explosions [*Dziewonski*, 1984; *Woodhouse and Dziewonski*, 1989; *Grand*, 1994; *van der Hilst et al.*, 1997]. These seismic tomography studies have delineated locations of upper and lower mantle velocity variations and have thereby provided the greatest detail on the internal structure of the Earth's mantle. *Forte et al.* [1993] use the *Morelli and Dziewonski* [1987] model of CMB topography for comparison with results of their preferred dynamic viscous mantle flow computations. That seismicity model has a depression in the CMB located below the subduction zones around the Pacific Ocean Basin and seemed to substantiate the dynamic topography solutions. *Forte et al.* [1993], however, also summarize the variability and inconsistencies in CMB topography between the various global tomographic solutions. They conclude that the seismic determination of CMB topography is an order of magnitude more difficult than mapping three-dimensional velocities in the lower mantle. To date, any topographic relief at the CMB (possibly 2–4 km) has not been identified with confidence. Thus the comparison of an induced CMB topography, related to a theoretical mantle viscous flow, with CMB topography inferred from seismic tomography is not presently reliable.

The more recent seismic tomographic images have indicated the penetration of subducted slabs into the lower mantle (deeper than 670 km). The seismic tomography solutions are commonly presented as sets of polynomial coefficients, for spherical shells for various depth ranges, with separate coefficients for *P* and *S* velocity variations. Surface seismic reflection and refraction observations also yield only velocity observations, but for shallow levels those velocities can be converted to density estimates with considerable confidence. This is because laboratory measurements on rocks likely penetrated by the seismic waves provide observations of that correlation. With increasing depths greater than 100 km, conversions of seismic velocities to density are increasingly uncertain.

One set of dynamic topography models assumed that the seismic tomography velocity variations are proportional to density but that inferred density variation was negatively correlated with the observed geoid [*Hager*, 1984; *Richards and Hager*, 1984; *Hager et al.*, 1985]. The models of these authors necessitated postulating surface, CMB, and possible internal chemical stratification at the 670-km seismic discontinuity in order to attain long-wavelength agreement (degrees 2–6) with the observed geoid (the agreement for degrees 4 and 5 was not good). They assumed a Newtonian, spherically symmetric viscosity distribution for mathematical tractability and tested the effects of varying viscosity as a function of depth only. Models with the lower mantle viscosity increased by a factor of 10 over that of the upper mantle viscosity produced the best agreement for degrees 2–6. For that viscosity difference, with or without the chemical stratification at 670 km, those models matched more than 80% of the variance in the observed degree 2–3 geoid. Because the degree 2–3 geoid dominates the 2–10 geoid (see Plates 2 and 3 and later discussion), it also dominates the degree 2–6 geoid field [see also *Bowin*, 1991, Figures 2 and 4]. The predicted degree 2–6 dynamic topography for their best geoid fit has a surface equatorial positive relief of over 750 m in the central Pacific and northern Africa and a CMB positive relief at the same locations of over 1500 m.

In part, some of the difficulties in unambiguously demonstrating the validity of the dynamic tomography models rests with the inconsistency of the tomographic models used. Another problem is that different viscosity-depth assumptions commonly showed little variation in the dynamic topography results. Also, the basic problem of estimating viscosity and density from the seismic velocity variations of the tomographic solutions remains an inherent hurdle. *Hager and Richards* [1989] used least squares inversion to estimate the velocity-density parameter that fits the geoid. Integral to a test of the dynamic solutions are deformations of the Earth's surface and internal density boundaries, such as a chemical boundary at 670-km depth (particularly if upper mantle convection is distinct from lower mantle convection) or the CMB if there is whole mantle convection. The calculated surface deformations were originally too great and required modeling that would force a greater proportion of the dynamic topography to the deeper, less well defined, 670-km and CMB horizons, by adjusting viscosity variations at depth.

Seismic tomographic models continued to improve in resolution during the 1980s and 1990s, due to better ray coverage. They began showing more consistent definition of high-velocity subduction slabs, with evidence that at least in some places, they penetrate into the lower mantle [*Creager and Jordan*, 1986; *Grand*, 1994; *van der Hilst et al.*, 1997; *Grand et al.*, 1997].

A variety of studies on boundary deformation induced by flow [*Morgan*, 1965; *McKenzie*, 1977; *Parsons and Daly*, 1983] and the effects of viscosity stratification and layered convection in the mantle [*Hager and O'Connell*, 1981; *Richards and Hager*, 1984; *Ricard et al.*, 1993b] have shown that significant alterations of the calculated relationship between geoid heights and driving density contrasts could occur. Thermally driven convection in the mantle has been assumed. This is because thermal conduction of heat from the core, radiogenic heat production in the mantle, volcanic activity, solidifying of elevated oceanic crust at spreading centers, and subduction of cold lithosphere indicate a high probability of thermal disequilibrium. Anomalous high temperatures beneath spreading centers are generally considered to only persist to about 200-km depth [*Gaherty et al.*, 1999; *Ekström and Dziewonski*, 1998], so that mantle convection may be dominated by the sinking of cold subducted slabs. The deep internal temperature structure of the mantle and the deep temperature dependence of density and viscosity are imprecisely known.

Another method of evaluating mantle heterogeneity is by modeling the geometric history of subducted slabs [*Ricard et al.*, 1993b; *Lithgow-Bertelloni et al.*, 1993; *Lithgow-Bertelloni and Richards*, 1995, 1998]. This subduction modeling is argued to be equivalent to mapping the main thermal flux of the mantle, because mantle plumes (hotspots), which may originate near the CMB, appear to contribute only about 10% of the total flux [*Davies*, 1988; *Sleep*, 1990]. The subducting material was modeled as a collection of bloblets (5° cubic elements of subducted slab) that sink vertically (for simplicity) during sequential time intervals. The bloblets sink through time to deeper levels, dependent upon the assumed radial viscosity variations in the mantle. Plate motions appear to be in dynamic equilibrium (i.e., nonaccelerating), so they assume that the net torque acting on each plate is zero. For each plate they solve for the three-component Euler rotation vectors as a function of basal shear stress on each plate that would be excited by internal density heterogeneities, position vector, and the area of the plate. A propagator matrix solution to basal shear stresses on each single plate in the absence of internal loads is then obtained. The integral of these plate basal shear stress relations for zero net torque provide a solution for the load (mass distribution) that matches that for zero net torque. They base their density heterogeneity model on a subduction history by utilizing plate boundary and hotspot frame rotation vector sets for six Cenozoic and five Mesozoic time intervals. Because the positions of the subduction zones change from stage to stage, an effective dip angle for the bloblets becomes introduced during the plate stage reconstructions. Following *Ricard et al.* [1993b], the density contrast between bloblet and mantle is assumed to be 0.08 g cm^{-3}, with the surface density contrast modified by the square root of crustal age, in millions of years, divided by 90 (analogous with calculating seafloor depth from its crustal age in millions of years).

This subduction bloblet model of density heterogeneity of the mantle is tested in two ways. The first is with seismic tomography models, S12WM13 [*Su et al.*, 1994] and Saw12D [*Li and Romanowicz*, 1996]. They find the global correlation between their preferred slab model at all depths and seismic tomography is significantly lower than the correlation between the two tomographic models, although correlation coefficients are high for spherical harmonic coefficient comparisons for the degrees they considered. The second test was a comparison with the geoid. They obtain the best fit to the geoid anomalies (referenced to the hydrostatic figure) with a lithosphere that is 10 times more viscous than the upper mantle and a lower mantle that is 50 times more viscous than the upper mantle. A slowing factor of 4 was used (i.e., slab falling velocities in the lower mantle were assumed to be 4 times slower than in the upper mantle). They obtain an overall correlation with the nonhydrostatic geoid of 0.92 and a total variance reduction of 86%. The correlation coefficients are very close to 95% for degrees 2, 6, and 9 and considerably above 95% for degrees 3, 4, and 5. The amplitude of the surface dynamic topography produced by their preferred slab model is rather large (about -2600 to $+1500$ m) and approximately coincident, but of opposite sign, with the positive slab geoid anomalies of degrees 4–10. Having part of the dynamic topography develop at the 670-km horizon could reduce the surface response by a factor of 2–3 [*Thoraval et al.*, 1995]. However, the increased viscosity used for the lower mantle was in itself a way of shifting a greater proportion of the surface dynamic topography (compensation) for the positive mass of the bloblets to greater downward deflection of the CMB.

6. MAGNITUDE OF DYNAMIC TOPOGRAPHY

Although the process of dynamic topography is well understood, the actual magnitude of such topography remains in question. *Colin and Fleitout* [1990], from a careful study of Earth topography data, claim that the surface dynamic topography is actually zero. They find no noticeable correlation between residual sediment-corrected topography and the geoid, except for a slight correlation for degree 6. Specifically, for degrees 2 and 3 the correlation is zero. By considering the evolution of mantle convection as a function of time, *Jackson et al.* [1991] infer that an initial mass distribution (mantle heterogeneities) would be partially compensated by deforming the CMB, hence diminishing the surface geoid. Thus they conclude that lower mantle mass anomalies that could generate the Earth's strong low-degree geoid anomalies must be monopolar (but not identified) and not directly associated with CMB topography. This is because they assume that topography on the CMB must be either isostatically or dynamically compensated and therefore would contribute little strength to the observed potential power spectrum. *Richards and Hager* [1984, Figure 1] illustrate by a convective flow model of degree 3 in which an upper mantle flow in the opposite direction to the flow in the lower mantle may reverse the sign of geoid anomalies above mass anomalies in the lower mantle. They also conclude that for uniform mantle viscosity, the geoid signature due to boundary deformation may be larger than that due to internal loads.

Dynamic topography of the Earth's surface should be the compensation boundary most readily testable, although glacial rebound and other factors can complicate its identification. Perhaps, also, the convection flow in the uppermost and lowermost mantle might be spread over greater regions (reducing the magnitudes of deflections) than might be assumed from the simple picture of downward deflections of the surface and CMB directly associated with a sinking positive subducting mass, implied by early dynamic topography solutions [e.g., *Hager*, 1984, Figure 2 or 5]. Presumably, if the scale of mantle convection is larger, then the deflections for the surface, CMB, 670-km, and other horizons would be broader and of lower amplitude. The pattern of convection in the mantle remains unknown. Helping to define that pattern has been a goal of the dynamic topography solutions. Perhaps, also, the driving mass of the subducting slab might be much smaller than has been modeled, hence resulting in only very minor deflections.

7. EARTH MASS ANOMALY MODELS

C. Lithgow-Bertelloni provided the author with a set of 9274 bloblets (i.e., central three-dimensional locations for the 5° cubic region of each bloblet) derived from her reconstructed plate subduction history [*Ricard et al.*, 1993b; *Lithgow-Bertelloni et al.*, 1993]. These data provide the best estimate of the volumetric locations of subducted material to date. We took advantage of these volumetric locations to test if we could generate a "static model" that might explain the regional geoid and gravity anomalies. The initial value of density contrast 0.08 g cm^{-2} assigned by *Ricard et al.* [1993b] to fit the dynamic topography is not relevant to our purpose. In fact, the absolute value of the density contrast has no physical significance at all, since even the reference mass distribution is rather ambiguous within the subduction zone areas. Therefore we treat the density contrast as an unknown free parameter to be determined by the best fit of our model to the observed geoid field. (This matter of the slab density anomaly is discussed further later.) Note that the volume of each bloblet (and hence its mass) because of geometric effects decreases with latitude away from the equator and with depth into the Earth. The Lithgow-Bertelloni bloblet data set provides slab location estimates at 20 different depths. Plate 4 shows their spatial distributions at eight selected depths. Note the paucity of points in the eastern Pacific for depths shallower than 550 km. Note also that the number of bloblet locations increases substantially with depth, whereas that increase would not be evident from the mantle density heterogeneity model schematic illustration of *Lithgow-Bertelloni and Richards* [1998, Figure 6]. A static bloblet slab model (with density of 0.0004 g cm^{-2}) using all the bloblets accounts only crudely for Earth geoid data (Plate 5, degree 2–10, but without hydrostatic flattening). Increasing the bloblet density slightly would improve the geoid magnitudes, but their patterns would remain the same. The total bloblet model shows that approximately 65% of its total mass lies in the mantle below 800-km depth (Figure 14a). CCC data for the New Guinea geoid high of this bloblet model (not shown) differ from the real Earth by not having a sharp change in slope between the 2–3 and 4–10 degree packets (Plate 2). For example, this total bloblet model has only a 70.15% percentage CCC value at degree 3 for the New Guinea geoid high. However, a dynamic topography solution set of spherical harmonic coefficients (degrees 2–20) from these same bloblet data was received from Y. Ricard [*Ricard et al.*, 1993b]. Ricard et al. demonstrate a good match to the Earth's hydrostatic geoid anomalies (Plate 6) and show an 83.5% degree 3 CCC value for its New Guinea geoid high. This comparison indicates that dynamic topography solutions have the effect of involving the greater mass distribution in the lower mantle to induce topography at the CMB. Figure 15 shows the percentage CCC plots for South American and New Guinea geoid highs from the *Ricard et al.* [1993b] dynamic topography solution. Note the lack of consistent estimated equivalent point-mass depths at the South American Andes site.

Having bloblet data with which to experiment has been extremely useful. Some refinements will probably prove useful in the future. For example, we note that no bloblets are indicated for the South American Andes subduction zone until depths greater than 600 km (Plate 4). With the existing set we could test what spherical harmonic contributions arise from different bloblet depth ranges and hence try to converge to what mass distribution might provide the observed sharp distinction between the degree 2–3 and 4–10 packets. On the basis of our 800- and 1400-km mass models, and the *Ricard et al.* [1993b] coefficients, we conclude that such a sharp distinction can be expected whenever deep mass anomalies strongly dominate a planet's geoid field. The greater mass source (~65% or more) could be distributed in the lower mantle (as in the dynamic topography solution) or concentrated at the CMB (as presented here), with a lesser total mass source (~35% or less) resulting from slab masses high in the mantle. The question remains, What is the origin of the Earth's great deep mass anomalies?

Our best model with bloblets restricted to depths less than 800 km (s800gb3NSIC) has reduced density of 0.0004 g cm^{-3} but with a sixfold density increase for those bloblet masses at depths greater than 670 km to simulate slab material piling up beneath the 670-km discontinuity. Four masses at the CMB were also required to match the 3, 2–3, 3–10, and 2–10 geoid anomaly patterns (Plate 2, 800 km): 0.1000×10^{22}, -0.9422×10^{23}, 0.1100×10^{24}, and 0.7200×10^{23} g. One is beneath the New Guinea geoid high (which adds to the New Guinea geoid high contribution from the bloblet data). A second is a large negative mass anomaly beneath the Indian Ocean low and two positive masses beneath the Iceland and Crozet geoid highs, which are assumed to be related to hotspot plume initiation locations. In comparison with the CMB mass estimates by the gravity over geoid ratio method (initial estimates of Figure 7), this New Guinea value is about 13 times smaller, presumably because contributing slab contributions have been separated. The magnitudes of the other three CMB mass values used are only about 3 times greater than the initial *g*/*N* ratio estimates.

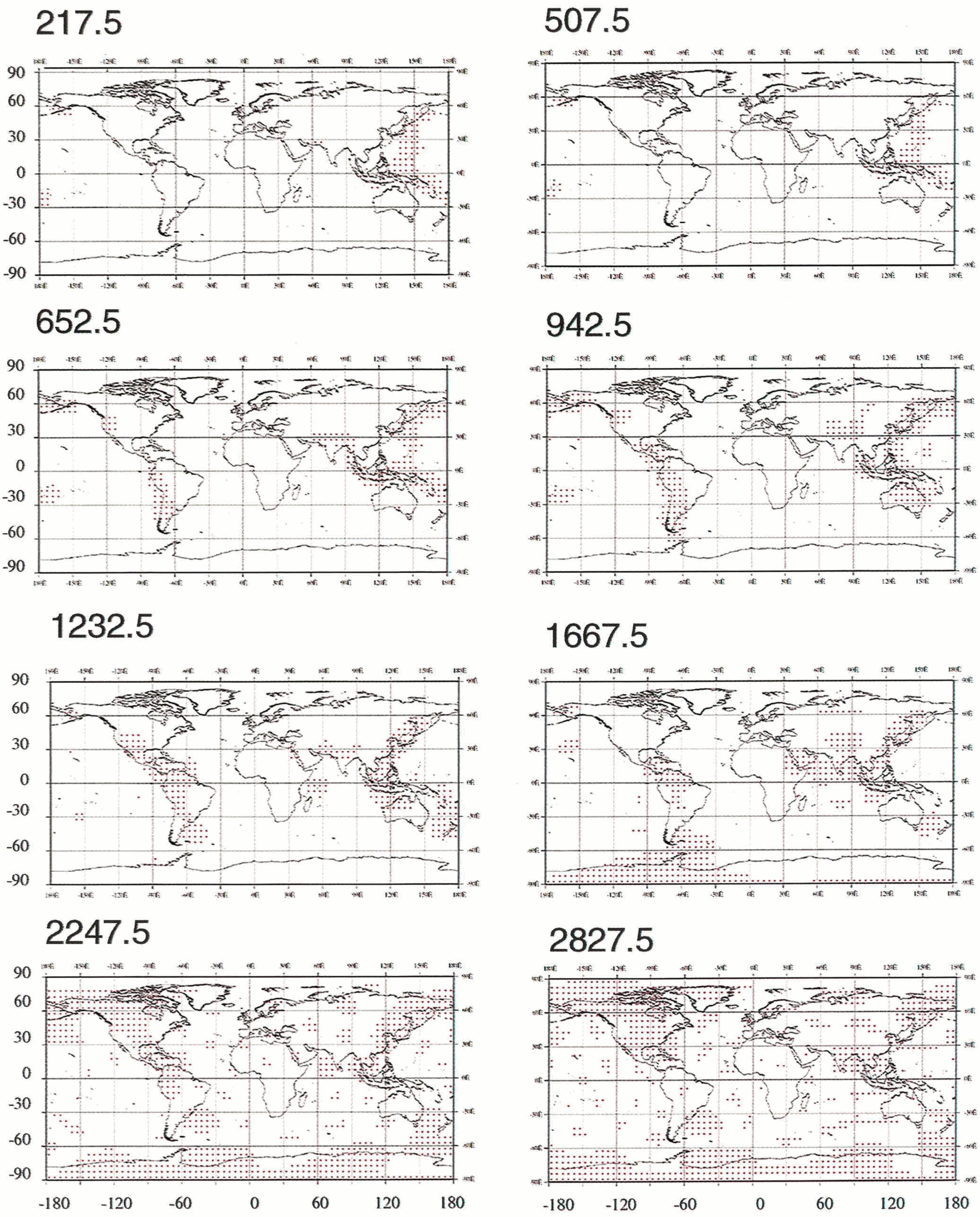

Plate 4. Global maps of bloblet locations for eight selected depths where their distribution changes the most. Data are from *Lithgow-Bertelloni et al.* [1993].

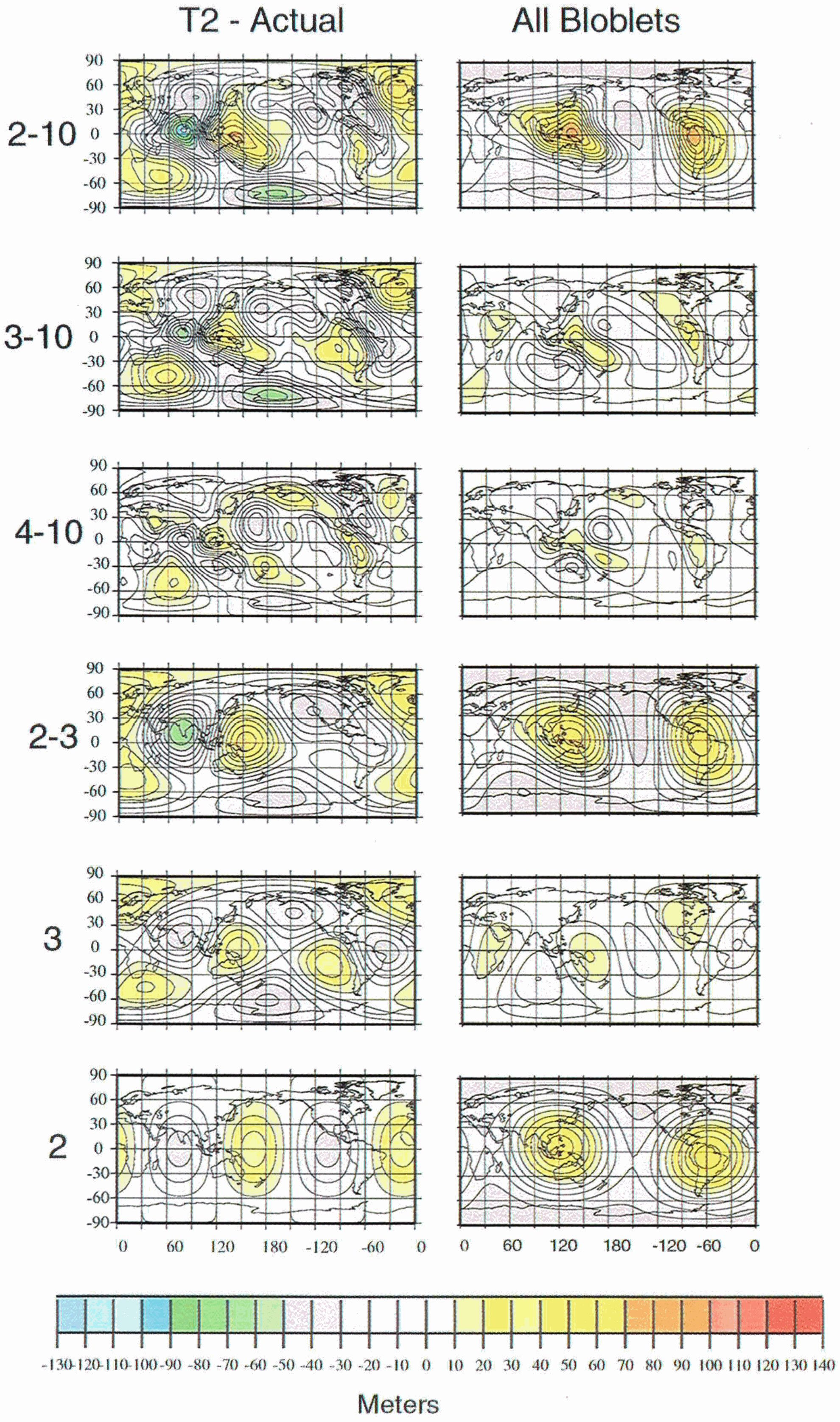

Plate 5. Global geoid anomaly maps from spherical harmonic coefficients GEM-t2 and computed from mass anomaly model with all bloblets from *Ricard et al.* [1993b] and *Lithgow-Bertelloni et al.* [1993] using a bloblet density of 0.0004 g cm^{-2}. Maps are for degrees 2–10, 3–10, 4–10, 2–3, 3, and 2.

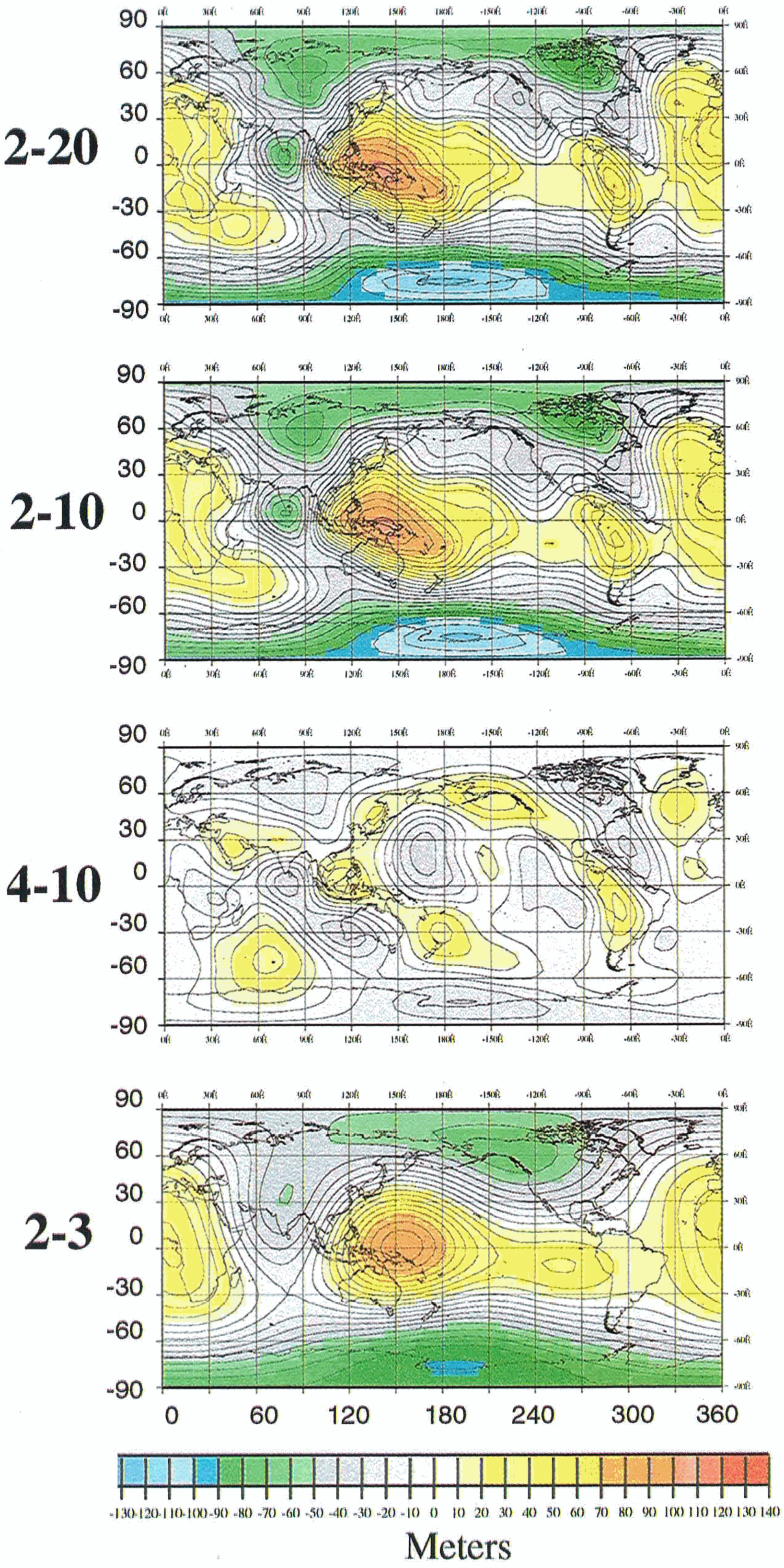

Plate 6. Geoid anomaly maps prepared from the dynamic topography hydrostatic solution spherical harmonic coefficients computed by *Ricard et al.* [1993b] from the total bloblet data set of *Lithgow-Bertelloni et al.* [1993]. These results show good correspondence with the hydrostatic flattening GEM-t2 maps shown in Plate 3.

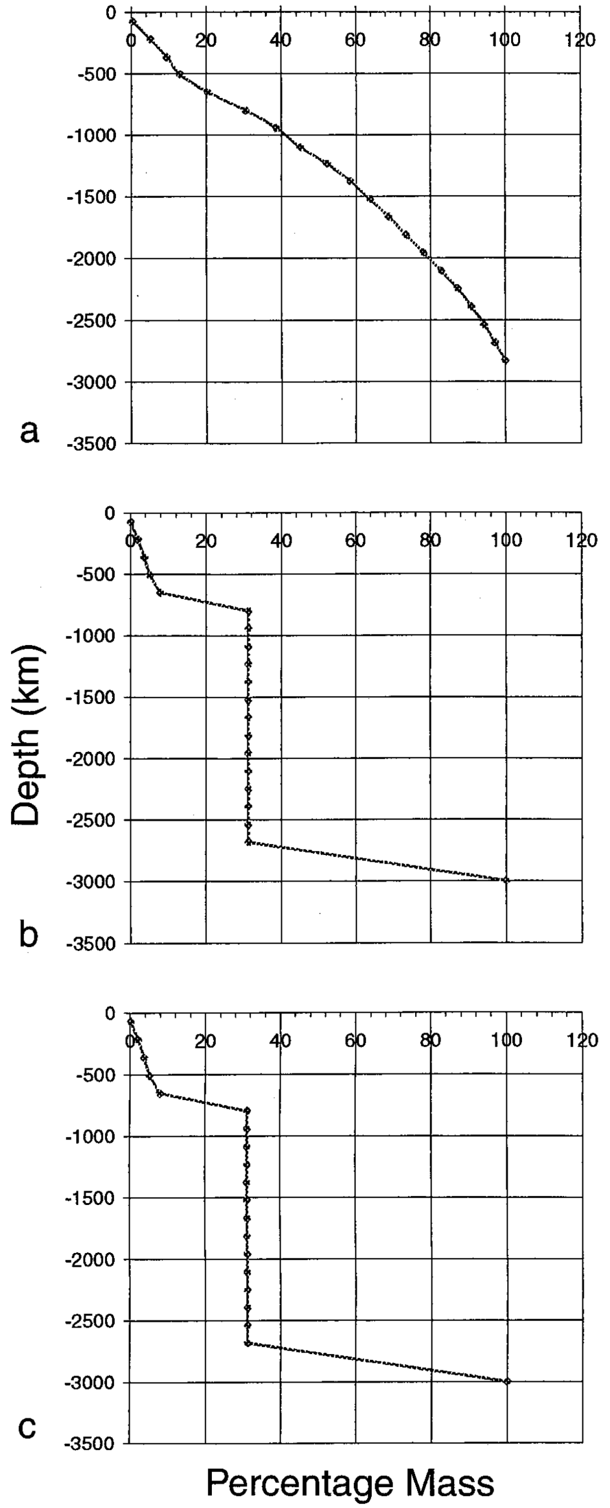

Figure 14. Cumulative percentage plots for anomalous mass of three Earth models. (a) All bloblet data from *Lithgow-Bertelloni et al.* [1993]. (b) The 800-km Earth mass model with four CMB point masses. (c) The 1400-km Earth mass model with the same four CMB point masses.

In order to test constraints on a slab model that penetrates into the lower mantle, as indicated by recent seismic tomography data, another model with slab bloblets continued to 1400-km depth was constructed. This model (s1400cdNSIC) utilizes the slab bloblets at 10 depth levels (72.5, 217.5, 362.5, 507.5, 652.5, 797.5, 942.5, 1087.0, 1232.0, and 1377.0 km), with respective densities of 0.000999, 0.000999, 0.0008658, 0.00005, 0.00225, 0.000666, 0.0008375, 0.000999, 0.0011655, and 0.001332 g cm^{-3}. Global maps for several degree packets for these models are given in Plate 2 (actual flattening) and Plate 3 (hydrostatic flattening) for both the 800- and 1400-km models. Since all masses contribute to all harmonic degree coefficients, one has to always compute harmonic coefficients for each total mass model trial (with both slab and CMB masses) for comparison with real Earth data. We were trying to match not only the degree 2–30 regional geoid field, but also the degree 2–10, 3–10, 4–10, 2–3, 3, and 2 anomaly patterns. The cumulative percentage mass distribution with depth is shown in Figures 14b and 14c for the 800- and 1400 km models, respectively.

To compare our mass models with the hydrostatic geoid pattern, we modified the model C_{20} coefficient values. As was cited before, this was done as if the main difference between the actual flattening and the hydrostatic flattening might simply be due to a delayed Earth response (of 10^7 years) to the slowing of its rotation rate [*O'Keefe and Kaula*, 1963]. The hydrostatic reference figure geoid results are shown in Plate 2 (800 and 1400 km). Again, there is a reasonably good agreement with the global patterns and magnitudes of the GEM-t2 geoid fields.

Although the global geoid patterns of the 800- and 1400-km models do not match perfectly to that of the real Earth, these models are offered as demonstrating that a restricted class of mass distributions appears to provide a promising solution for the Earth's regional equipotential field that does not invoke dynamic topography. This class has great mass anomalies at the core-mantle boundary and lesser mass anomalies limited to residing much higher in the mantle.

8. DISCUSSION OF SLAB DENSITY ANOMALY

It might be argued that the low bloblet densities found by our forward modeling are too low compared to the 0.08 g cm^{-3} introduced in dynamic topography solutions by *Ricard et al.* [1993b]. That high value was also adopted in subsequent studies, such as those by *Lithgow-Bertelloni and Richards* [1995, 1998]. This value presents an interesting conundrum, for if the slab bloblets are not dense enough, then requisite Earth viscosities would probably appear unrealistically small under dynamic topography solutions. Further, large slab mass anomalies are probably essential for driving sufficient negative dy-

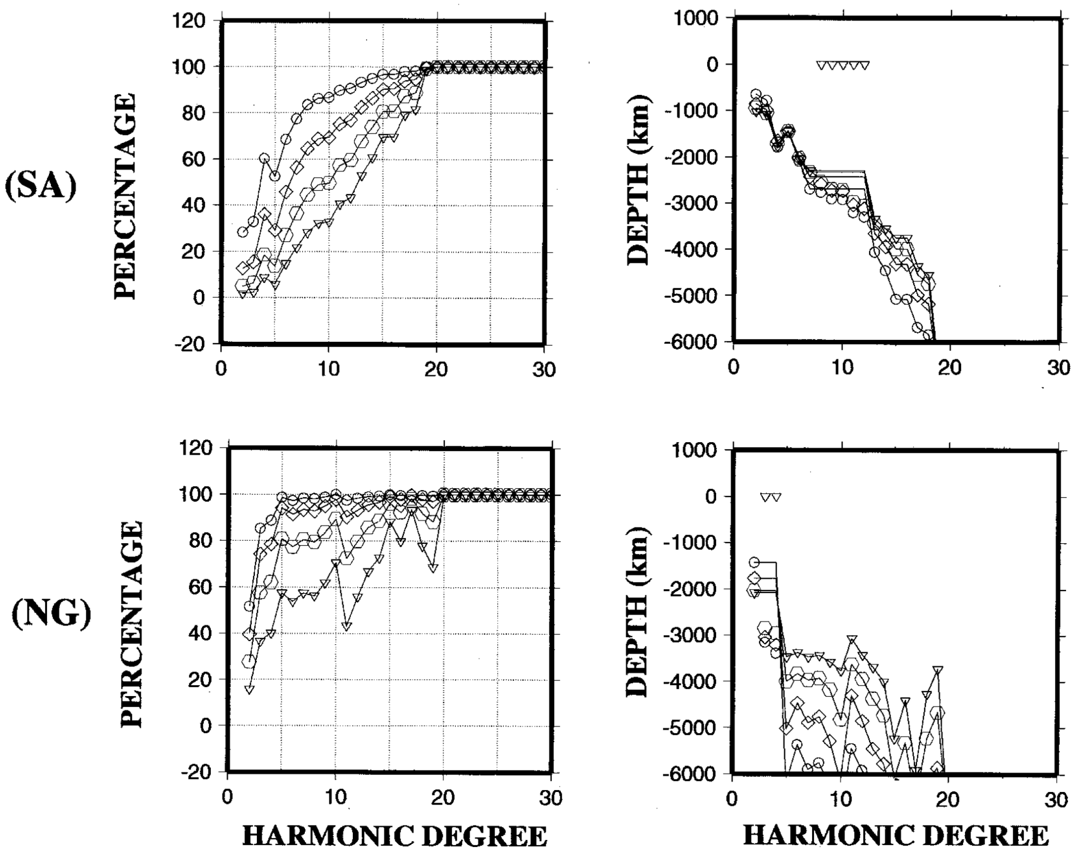

Figure 15. Percentage cumulative contribution curves, estimated equivalent point-mass depth, and estimated mass for the central locations of the South America geoid high (SA) and for the New Guinea geoid high (NG). Data are from spherical harmonic coefficients for the hydrostatic dynamic topography model of *Ricard et al.* [1993b].

namic topography at the surface, 670-km boundary, and CMB to overcompensate the positive mass contributions of the slabs themselves.

To estimate slab density, *Ricard et al.* [1993b, p. 21,897] derive what they call an "excess surface density" for ocean crust distant from spreading centers. They determined that value by assuming a 1000-K temperature jump across a 100-km-thick ocean lithosphere or, equivalently, a 3% $\Delta\rho/\rho$. The excess surface density relates to the thickening of the lithosphere as the nascent ocean crust cools as it moves away from the spreading center at which it was generated. Hence an increasing mass is assumed for the lithosphere as it thickens and displaces a lower density warm (hot) asthenosphere. *Hager and O'Connell* [1981] derive an average density contrast between lithosphere and the underlying asthenosphere of 0.0665 g cm^{-3} that satisfies the requirements of isostasy by taking the density contrast between seawater and the asthenosphere as 2.3 g cm^{-3}. Concomitant with this cooling and thickening of the lithosphere, the ocean floor is presumed to subside by amounts directly proportional to the increase in thickness of the lithosphere. *Parker and Oldenburg* [1973] calculate that thickness to attain 100 km at 120 Ma. *Molnar et al.* [1979] estimate a slightly greater thickness over all ages to about 110 km at 140 Ma. For ages less than about 70 Myr, *Parsons and Sclater* [1977] give the function for ocean floor depth (in meters) as $d = 350 \times t^{0.5}$, with t being crustal age, in millions of years. Beyond this age the subsidence is less rapid.

Colin and Fleitout [1990] empirically examined sediment-corrected seafloor depths and noted that because of the large scatter of corrected seafloor depths, the topography when averaged by 10-Myr intervals shows a beginning of depth flattening at 40 Ma (their Figure 1). *Hager and O'Connell* [1981] discuss a number of explanations why the flattening of the seafloor depth curve might depart from simple boundary-layer theory. These are that heat is supplied to the base of the lithosphere by small-scale convection [*Richter*, 1973; *Richter and Parsons*, 1975; *McKenzie and Weiss*, 1975; *Parsons and McKenzie*, 1978]; by plumes [*Heestand and Crough*, 1980]; by viscous heating [*Schubert et al.*, 1976]; by variations of thermal properties with depth and radioactive heating [*Forsyth*, 1977]; or by heat generation anywhere in the upper mantle [*O'Connell and Hager*, 1980]. *Oxburgh and Turcotte* [1978] and *Schubert et al.* [1978] alternatively suggest that the boundary-layer thermal model may be correct, with isostatic compensation prevented by dynamic effects. On the other hand, if the mantle below the plate were cooled by small-scale convection or conduction, the density of the sublithosphere mantle would increase and result in a density contrast not accounted for by the plate model.

Except at deep-sea trenches, sites of plate convergence (subduction zones), ocean crust is normally in isostatic equilibrium. Isostatic equilibrium is indicated by the general range of ocean free-air gravity anomalies within a range of ±20 mGal (see Figure 5). Thus sections of ocean crust 100–200 km thick practically everywhere have the same total mass. The decay of heat flow values away from spreading centers is strong evidence that the decrease of ocean topography away from spreading centers (and with increasing crustal age) results from thermal decay of extra heat input at the spreading center. Perhaps old ocean crust (>70 Myr) is "normal" for the Earth's thermal equilibrium and that the shallow topography at spreading centers is "abnormal" due only to thermal expansion from added heat sources there. The extent to which sections of ocean lithosphere are "top-heavy" (have an excess surface density) does not relate to whether or not subduction takes place. After all, a spreading center on the Juan de Fuca plate is being subducted now [*Gordon and Stein*, 1992, Figure 1]. What triggers initiation of subduction remains a problem, but "heavy" ocean lithosphere does not just fall (sink) anywhere into the mantle.

The slab mass density increases in our models below 670 km, and P wave amplitude increases below 670 km [*Gaherty et al.*, 1991, Figure 1b; *Fischer et al.*, 1988, Figure 1], both suggest that lower mantle portions of subduction zones have greater effects on continued subduction than do upper mantle portions. A similar conclusion, that slab material in the lower mantle appears to be essential for achieving models of plate-driving forces, is stated by *Lithgow-Bertelloni and Richards* [1998, p. 63]. *Forsyth and Uyeda* [1975] explain that the slab/mantle density contrast is small at shallow depths because of the small density difference between the slab and the surrounding mantle. That density contrast, they state, will increase with depth until the heating of the slab becomes significant and will be enhanced greatly at a depth of 200–300 km, where the olivine-spinel transition takes place in the slab. What may produce the greater slab masses in the upper part of the lower mantle is not yet resolved, although phase changes may be a cause. Because locations of subduction zones, in an absolute frame of reference, have remained consistent for the past 130 Myr, we infer that factors other than the magnitude of excess surface density have more significance. Therefore solving for slab densities by forward modeling continues to seem a reasonable procedure.

9. TESTS

We also tested how well our Earth mass models approximated the South American and New Guinea regional geoid anomaly percentage CCC patterns (Figure 16). The hydrostatic Earth mass model percentage CCC and estimated equivalent point-mass depth curves for the 800- and 1400-km-model South American and New Guinea geoid highs are shown in Figure 16 for comparison with Figure 22. The comparison is reasonably good for the 800-km model but poor for the 1400-km model.

These Earth mass anomaly models of 909 point masses (800 km) and 1520 point masses (1400 km) are the most detailed known that do not involve viscosity assumptions about the mantle. Both have reasonable agreement with the patterns and magnitudes of several geoid anomaly component degree ranges (Plates 2 and 3), as does the dynamic topography solution of *Richard et al.* [1993b] (Plate 6). However, the dynamic topography contribution induced by the bloblets in our two models is probably very small. This is because the slab densities found in our two forward models are about 200 times smaller than that inferred in the dynamic topography solutions, and fewer bloblets are involved. Note also that the degree 3, 3–10, and 4–10 patterns are not dependent upon the C_{20} flattening coefficient. These initial Earth mass models are offered as a demonstration that the Earth's geoid can be realized without invoking dynamic topography. However, just as the dynamic topography solutions had to make ad hoc choices for mantle viscosity variations and slowing factors, our models also require some presently unsubstantiated mass sources at the CMB. Such mass sources are likely to result if there is isostatically uncompensated (by mantle anomalies) topography at the CMB, Earth's greatest density boundary. Such CMB topography, of course, might be compensated by mass distribution or dynamics within the core. *Jackson et al.* [1991] noted that mantle dynamically generated CMB topography would serve to diminish geoid anomalies, by partial compensation of the mobile mantle heterogeneities, rather than generate them. Therefore they inferred that lower mantle mass anomalies that possibly generate the low-degree spectral strength of the Earth's potential field must be largely monopolar. Since they assume that topography at the CMB must be either isostatically or dynamically compensated, such topography, they contend, would contribute little strength to the geoid field. Traditionally, CMB topography has been considered critically important because of the great disparity of viscosity between mantle and core. Thus the hypothesis of mantle-invoked dynamic topography provided a means of explaining why the Earth's total geoid (degrees 2–10) shows virtually no relationship to plate tectonics, whereas degrees 4–10 have an excellent agreement with sites of subduction. To accept the dynamic topography solution, one must be satisfied with proposed viscosity variations that will bring about compensating deflections that dwarf the magnitude of the driving subducting masses. One must also accept an apparently large density value (0.08 g cm^{-3}) for subducted slab material.

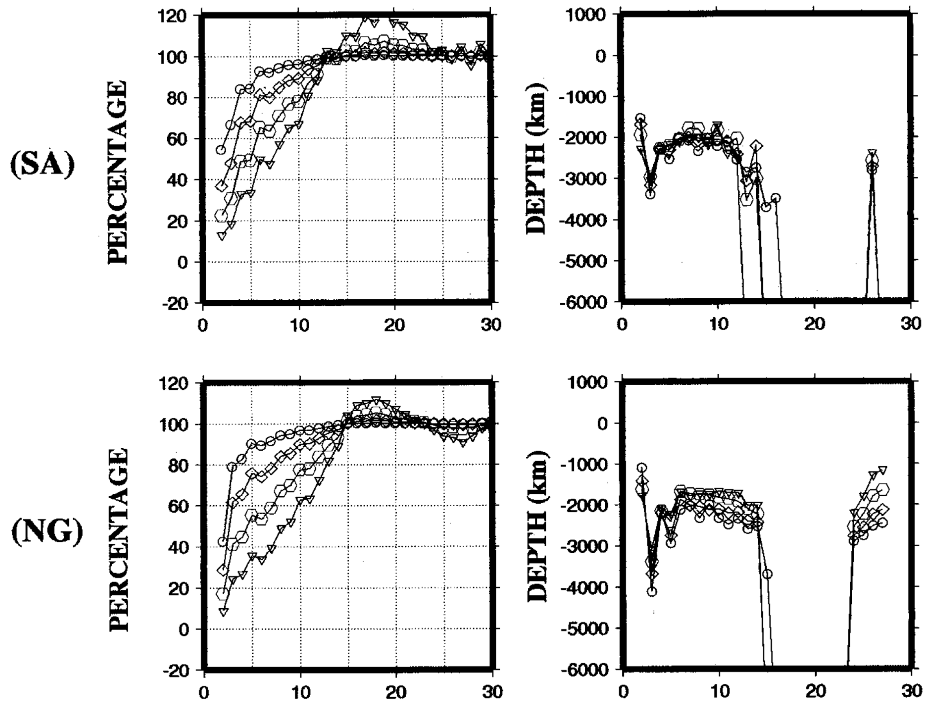

a 800 km Model

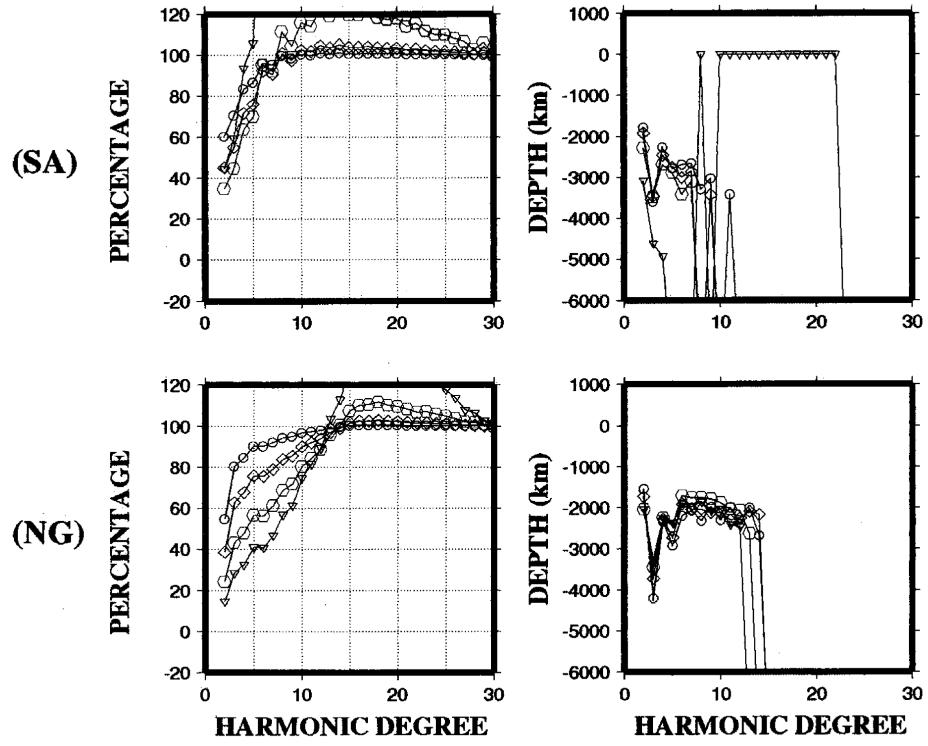

b 1400 km Model

Figure 16. Percentage cumulative contribution curves, estimated equivalent point-mass depth, and estimated mass for the central location of the South America geoid high. (a) The 800-km mass model. (b) The 1400-km mass model.

The present author has taken the same observations but concluded, because of the pronounced change in geoid pattern between 4–10 and 3–10 when the degree contributions are added backward [see *Bowin*, 1991, Figures 2 and 4], and since the 4–10 geoid positive anomalies coincide so well with sites of subduction, that two different mass anomaly sources probably contribute to the Earth's geoid. Deeper, greater mass anomalies at the CMB unrelated to plate tectonics are the main contributors to degrees 2–3, and lesser, shallower mass anomalies related to plate subduction zones are the main contributors to degrees 4–10. The percentage CCC data for the South American and New Guinea regional geoid highs support this view (Figure 13), as do the two mass anomaly models presented here (Plates 2 and 3). The CMB masses used in the models are of the same order of magnitude as those estimated by g/N ratios (Figure 7). Having the Earth's greatest mass anomalies at the CMB also helps explain the differences in the CCC diagrams (Figure 3) among Earth, Venus, and Mars [*Bowin*, 1998]. All three planets have metallic cores, but for Mars and Venus, surface topographic features correlate with these planets' greatest geoid anomalies, and the author expects their core-mantle boundaries to be relatively smooth. Venus rotates very slowly, has no magnetic field, and therefore lacks a requisite core convection. Only the Earth is unique in having its greatest mass anomalies deep within the planet.

10. MAGNITUDE OF DRIVING FORCE FOR PLATE TECTONICS

As we all learn in introductory physics, force equals mass times acceleration. Since the bloblet 800- and 1400-km data models provide an approximate match to the regional geoid anomalies of the Earth, it seems obvious that they could also provide an estimate of the driving force for plate tectonics, under the assumption that subducted slabs are indeed the principal driving force. Following our assumption that processes within the Earth's core, not within the mantle, produce the mass anomalies resulting from topography at the CMB, we first had to remove the four mass points simulating CMB topography. The result was a collection of positive bloblet subduction masses in the mantle for which we had identified densities. By determining gravity acceleration values at the depths of each bloblet, and multiplying the gravity acceleration values by the bloblet mass, a force contribution due to each bloblet could be calculated. By summing these force contributions vertically at the center locations of the global 5° × 5° grid points, a map of the subduction force distribution at the Earth's surface could be prepared (see Plate 7). By summing all of the participating bloblets, we obtained an estimate of the total driving force for each model.

The Earth's internal gravity acceleration values were determined based on two estimates for the distribution of density as a function of depth. Note that no allowance for slab dip is made. One density-depth function is that defined by the preliminary reference Earth model (PREM) [*Dziewonski and Anderson*, 1981], the one generally used in seismological studies. The other density-depth function used is the common geodetic and geophysical model (CGGM) [*Denis et al.*, 1991]. The CGGM function has a much smaller density contrast at the inner core boundary (ICB) than the PREM. The CGGM has an inertia coefficient y of 0.332. A comparison of their density structures is given by *Denis et al.* [1997, Figure 1]. The PREM densities for the inner and outer cores are higher than those for the CGGM densities; however, the reverse (by a small amount) is the case within the lower mantle. They coincide for the upper mantle. Thus the acceleration due to gravity is higher in the lower mantle for the PREM but greater for the CGGM in the upper mantle. The PREM and CGGM density functions most likely bound the limits of that for the real Earth. Recall also that bloblet volumes decrease with depth. The estimates obtained are given in Table 1.

A dyne (cgs system) is the acceleration of 1 g 1 cm s^{-2}. One newton (mks system) is the acceleration of 1 kg 1 m^{-1} s^{-2}. Therefore 1 N is equivalent to 10^5 dyn. Hence the PREM estimates for plate driving force are 4.1×10^{20} N (800-km model) and 1.6×10^{21} N (1400-km model). The CGGM estimates are 2.8×10^{20} N (800-km model) and 3.2×10^{21} N (1400-km model). Prior estimates of the slab pull force have been made in terms of N m^{-1} of surface length subduction zone boundary, or as dyn cm^{-1}. Using the circumference of the Earth (40,000 km, 4.0×10^7 m, or 4×10^9 cm) as a close approximation for the maximum total trench length, we obtain the following PREM results: 1.0×10^{13} N m^{-1} (800 km) and 4.0×10^{13} N m^{-1} (1400 km). For the CGGM the results are only slightly different: 7.0×10^{12} N m^{-1} (800 km) and 8.1×10^{13} N m^{-1} (1400 km).

The 800-km PREM value is the same order of magnitude as estimated by *England and Wortel* [1980, Table 2] for the total resisting force for subduction for older aged ocean lithosphere. The PREM results, similarly, agree with the force per unit length of 10^{15} dyn cm^{-1} calculated by *Molnar and Grey* [1979] for a plate 100 km thick. Both these cited studies utilized and extended the thermal analytical subduction solution of *McKenzie* [1969]. As can be seen by the force values in Table 1, the CGGM Earth density models are about 70% of the PREM value for the 800-km model but twice the PREM value for the 1400-km model. It is perhaps very significant to note that these compatible driving force estimates are obtained from the 800- and 1400-km models that have estimated low densities for the subducted slab material (bloblets). Had a 0.08 g cm^{-3} bloblet density contrast been used instead, the estimated driving forces would have been 200 times greater and considerably exceeded the estimates derived from thermal considerations. A future study of the requisite parameters for

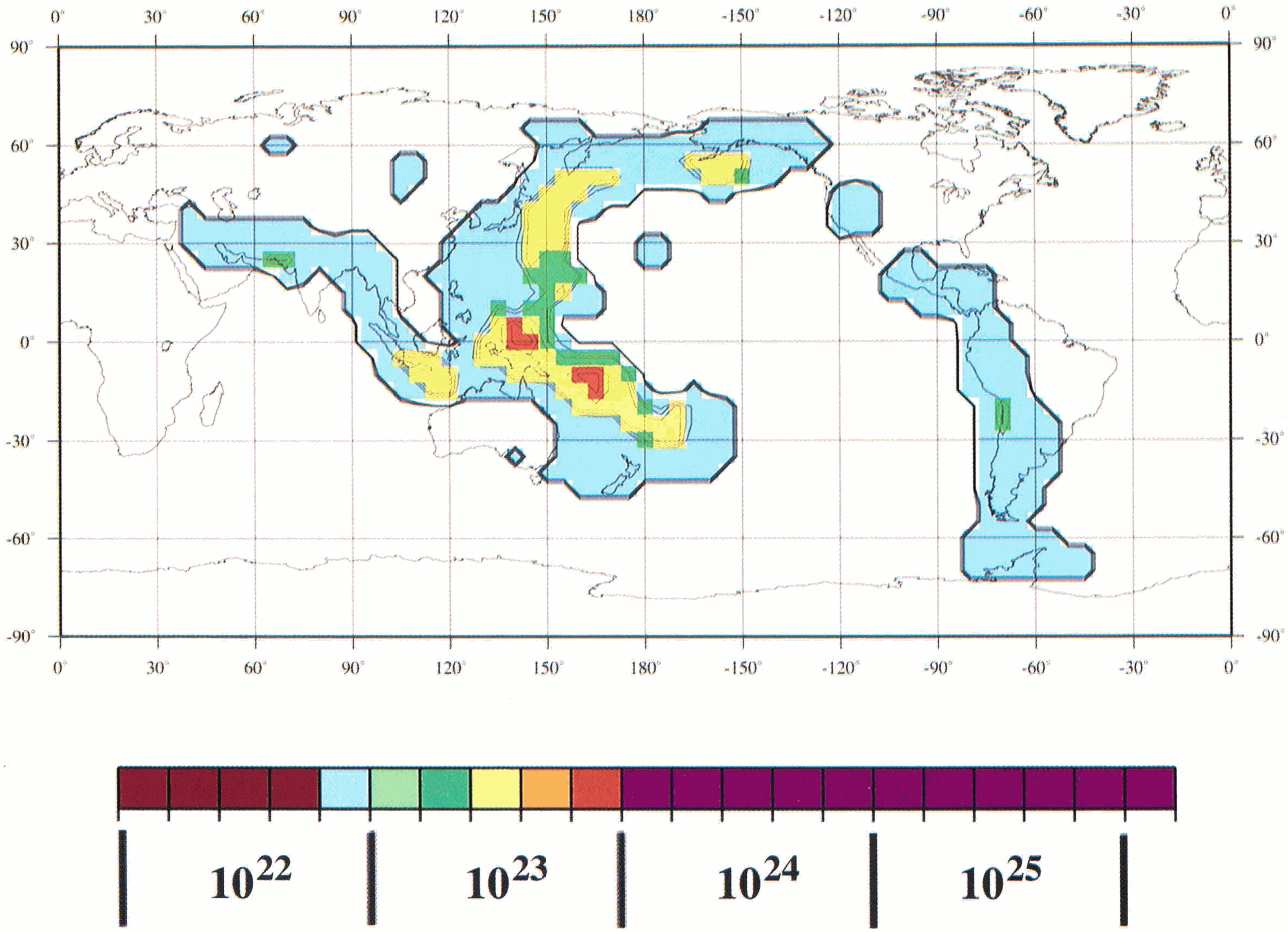

Plate 7. Map of plate tectonic driving forces from vertical sums of slab bloblets in a global 5° × 5° grid. These values were calculated using the common geodetic geophysical Earth density model [*Denis et al.*, 1997]. Force values computed with the preliminary reference Earth density model are only slightly smaller in magnitude.

TABLE 1. Estimates of the Plate Driving Force

	Preliminary Reference Earth Model	*Common Geodetic Geophysical Model*
800-km model	4.1430×10^{25}	2.7732×10^{25}
1400-km model	1.5889×10^{26}	3.2295×10^{26}

Values are given in dynes.

these two subduction models to produce observed plate motions would be interesting and might help in further judging the solution of the Earth's mass anomaly structure.

11. CORE-GENERATED CMB MASS ANOMALIES

What might produce the independent CMB mass anomalies? It is hypothesized that to conform with their independence from plate tectonics, CMB mass anomalies are presumably generated by processes within the core. Although core interactions with lateral variations in lowermost mantle properties, below an upper mantle–lower mantle convection regime, is an alternate view, it is considered an unlikely possibility because of the apparent lack of significant mass anomalies in the lowermost mantle. At present, we can only suspect that the momentum of internal core motions, and/or electromagnetic flux perturbations from main field, or outer core convection that may account for secular magnetic field variations, might produce the 2–4 km of CMB relief inferred from the magnitudes of the regional geoid anomalies.

In conclusion, this study has developed by forward testing two mass anomaly models that show reasonable correspondence with the Earth's regional degree 2–10 geoid and its degree components. These models utilized a set of three-dimensional locations (bloblet center points) that estimate subduction history in the mantle for the last 120 Myr of plate motions. Only those center points that are above 800-km depth were used by one model, and only those above 1400-km depth were used in the other. All deeper mantle bloblets were ignored. Instead, inferred topography at four locations on the CMB are modeled by four point masses at 3000-km depth. These two models were constructed to test the hypothesis that topography at the CMB generates the great harmonic degree 2 and 3 contributions to the Earth's gravity potential field and, further, that such CMB topography might be produced by processes within the core rather than within the mantle. Such an hypothesis would easily explain why the positive geoid anomalies of 4–10 harmonic degrees are overwhelmed by the 2–3 contributions to make a 2–10 geoid that shows no relation to the Earth's topography, magnetic field, or plate tectonics. The fourth greatest positive regional geoid anomaly, over the South American Andes, provides the strongest evidence that dynamic topography solutions require reexamination. The low magnitude of slab densities identified by our forward modeling are about 200 times smaller than those used in dynamic topography modeling. The low slab densities of the models presented here yield driving force estimates that agree with prior force estimates based on thermal modeling. This agreement further suggests the possibility that the dynamic topography solutions had to overestimate subduction densities in order to effect sufficient deflection on the surface and CMB to produce the great degree 2–3 contributions of the Earth's gravity field. Additionally, questions regarding the Earth's proper hydrostatic flattening figure are discussed.

ACKNOWLEDGMENTS. I thank Carolina Lithgow-Bertelloni for providing a copy of her mantle bloblet data set. The development of the alternative mass anomaly models presented here would not have been practical without it. I thank Yanik Ricard for providing spherical harmonic coefficients of his bloblet dynamic topography solution for comparison. Carlo Denis provided a Pascal computer program for computing the acceleration due to gravity at depth within the Earth. I also thank Ming Fang, Kelsey Jordahl, Mark Behn, Steve Anderson, John Krauspe, Roger Goldsmith, Tom Bolmer, Anjan Chakrabarty, Deborah Shafer, and Eric Cunningham for assistance with computer program and operating system problems (UNIX and NT4.0) and *Wessel and Smith* [1991] for their free GMT-System software. Manuscript review comments by Ming Fang, Maurice Tivey, Bert Vermeersen, Peter Cargill, Mark Behn, Rob Sohn, Denis Carlo, and an anonymous reviewer have been very helpful and much appreciated. Support from the Woods Hole Oceanographic Institution senior scientist emeritus fund is gratefully acknowledged.

Roel Snieder was the Editor responsible for this paper. He thanks Bert Vermeersen and an anonymous reviewer for technical reviews and Peter Cargill for the cross-disciplinary review.

REFERENCES

Bowin, C., Caribbean gravity field and plate tectonics, *Geol. Soc. Am., Spec. Pap. 169*, 79 pp., 1976.

Bowin, C., Depth of principal mass anomalies contributing to the Earth's geoidal undulations and gravity anomalies, *Mar. Geod.*, *7*, 61–100, 1983.

Bowin, C., Global gravity maps and the structure of the Earth, in *The Utility of Regional Gravity and Magnetic Anomaly Maps*, edited by W. J. Hinze, pp. 88–101, Soc. of Explor. Geophys., Tulsa, Okla., 1985.

Bowin, C., Topography at the core-mantle boundary, *Geophys. Res. Lett.*, *13*, 1513–1516, 1986.

Bowin, C., Earth's gravity field and plate tectonics, *Tectonophysics*, *187*, 69–89, 1991.

Bowin, C., The geoid and deep Earth mass anomaly structure, in *Geoid and Its Geophysical Interpretations*, edited by P. Vanicek and N. T. Christou, 343 pp., CRC Press, Boca Raton, Fla., 1994.

Bowin, C., Mass anomalies of Earth, Venus, and Mars: Initial estimates, in *Gravity, Geoid, and Marine Geodesy: Proceedings of the International Symposium, Tokyo, Japan, September 30–October 5, 1996*, edited by J. Segawa et al., pp. 257–264, Springer-Verlag, New York, 1998.

Bowin, C., E. Scheer, and W. Smith, Depth estimates from ratios of gravity, geoid, and gravity gradient anomalies, *Geophysics*, *51*(1), 123–136, 1986.

Bullen, K. E., *The Earth's Density*, John Wiley, New York, 1975.

Colin, P., and L. Fleitout, Topography of the ocean floor: Thermal evolution of the lithosphere and interaction of deep mantle heterogeneities with the lithosphere, *Geophys. Res. Lett.*, *17*, 1961–1964, 1990.

Creager, K. C., and T. H. Jordan, Slab penetration into the lower mantle beneath the Mariana and other island arcs of the northwest Pacific, *J. Geophys. Res.*, *91*, 3573–3589, 1986.

Davies, G. F., Ocean bathymetry and mantle convection, 1, Large-scale flow and hotspots, *J. Geophys. Res.*, *93*, 10,467–10,480, 1988.

Denis, C., A. I. Denis-Karafistan, and C. Delire, Sur un modèle de référence terrestre commun à la géodésie et à la géophysique, in *Actes des Journées 1991*, *"Systemes de Reférénce Spatio-Temporels,"* edited by N. Capitaine, pp. 116–121, Obs. de Paris, Paris, 1991.

Denis, C., Y. Rogister, M. Amalvict, C. Delire, A. Ibrahim Denis, and G. Munhoven, Hydrostatic flattening, core structure, and translational mode of the inner core, *Phys. Earth Planet. Inter.*, *99*, 195–206, 1997.

Denis, C., M. Amalvict, Y. Rogister, and S. Tomecka-Suchon, Methods for computing internal flattening, with applications to the Earth's structure and geodynamics, *Geophys. J. R. Astron. Soc.*, *130*, 603–642, 1998.

Dziewonski, A. M., Mapping the lower mantle: Determination of lateral heterogeneity in *P* velocity up to degree and order 6, *J. Geophys. Res.*, *89*, 5929–5952, 1984.

Dziewonski, A. M., and D. L. Anderson, Preliminary reference Earth model, *Phys. Earth Planet. Inter.*, *25*, 297–356, 1981.

Ekström, G., and A. M. Dziewonski, The unique anisotropy of the Pacific upper mantle, *Nature*, *394*, 168–172, 1998.

England, P., and R. Wortel, Some consequences of the subduction of young slabs, *Earth Planet. Sci. Lett.*, *47*, 403–415, 1980.

Fischer, K. M., T. H. Jordan, and K. C. Creager, Seismic constraints on the morphology of deep slabs, *J. Geophys. Res.*, *93*, 4773–4783, 1988.

Forsyth, D. W., The evolution of the upper mantle beneath mid-ocean ridges, *Tectonophysics*, *38*, 98–118, 1977.

Forsyth, D. W., and S. Uyeda, On the relative importance of the driving forces of plate motions, *J. R. Astron. Soc.*, *43*, 163–200, 1975.

Forte, A. M., A. M. Dziewonski, and R. L. Woodward, Aspherical structure of the mantle, tectonic plate motions, nonhydrostatic geoid, and topography of the core-mantle boundary, in *Dynamics of the Earth's Deep Interior and Earth Rotation*, *Geophys. Monogr. Ser.*, vol. 72, edited by J.-L. Le Mouël, D. E. Smylie, and T. Herring, pp. 135–166, AGU, Washington, D. C., 1993.

Froidevaux, C., and B. L. Isacks, The mechanical state of the lithosphere in the Altiplano-Puna segment of the Andes, *Earth Planet. Sci. Lett.*, *71*, 305–314, 1984.

Gaherty, J. B., T. Lay, and J. E. Vidale, Investigation of deep slab structure using long-period *S* waves, *J. Geophys. Res.*, *96*, 16,349–16,367, 1991.

Gaherty, J. B., M. Kato, and T. H. Jordan, Seismological structure of the upper mantle: A regional comparison of seismic layering, *Phys. Earth Planet. Inter.*, *110*, 21–41, 1999.

Gibbons, G., Brane-worlds, *Science*, *287*, 49–50, 2000.

Goldreich, P., and A. Toomre, Some remarks on polar wandering, *J. Geophys. Res.*, *74*, 2555–2567, 1969.

Gordon, R. G., and S. Stein, Global tectonics and space geodesy, *Science*, *256*, 333–342, 1992.

Grand, S. P., Mantle shear structure beneath the Americas and surrounding oceans, *J. Geophys. Res.*, *99*, 11,591–11,621, 1994.

Grand, S. P., R. D. van der Hilst, and S. Widiyantoro, Global seismic tomography: A snapshot of convection in the Earth, *GSA Today*, *7*, 1–7, 1997.

Greene, B., *The Elegant Universe*, 448 pp., W. W. Norton, New York, 1999.

Hager, B. H., Subducted slabs and the geoid: Constraints on mantle rheology and flow, *J. Geophys. Res.*, *89*, 6003–6015, 1984.

Hager, B. H., and R. J. O'Connell, A simple global model of plate dynamics and mantle convection, *J. Geophys. Res.*, *86*, 4843–4867, 1981.

Hager, B. H., and M. A. Richards, Long-wavelength variations in Earth's geoid: Physical models and dynamic implications, *Philos. Trans. R. Soc. London.*, *Ser. A*, *328*, 309–327, 1989.

Hager, B. H., R. W. Clayton, M. A. Richards, R. P. Comer, and A. M. Dziewonski, Lower mantle heterogeneity, dynamic topography, and the geoid, *Nature*, *313*, 541–545, 1985.

Heestand, R. L., and S. T. Crough, The effect of hotspots on the empirical age-depth relation, *Eos Trans. AGU*, *61*, 380, 1980.

Jackson, M. J., H. N. Pollack, and S. T. Sutton, On the distribution of anomalous mass within the Earth: Forward models of the gravitational potential spectrum using ensembles of discrete mass elements, *Geophys. J. Int.*, *107*, 83–94, 1991.

Jordan, S. K., Statistical model for gravity, topography, and density contrasts in the Earth, *J. Geophys. Res.*, *83*, 1816–1824, 1978.

Kaula, W. M., Theory of statistical analysis of data distributed over a sphere, *Rev. Geophys.*, *5*, 83–107, 1967.

Lambeck, K., Lateral density anomalies in the upper mantle, *J. Geophys. Res.*, *81*, 6333–6340, 1976.

Lerch, F. J., S. M. Klosko, R. E. Laubscher, and C. A. Wagner, Gravity model improvement using Geos 3 (GEM 9 and 10), *J. Geophys. Res.*, *84*, 3897–3916, 1979.

Lerch, F. J., S. M. Klosko, and G. B. Patel, A refined gravity model from Lageos, *Geophys. Res. Lett.*, *9*, 1263–1266, 1982.

Li, X., and B. Romanowicz, Global mantle shear velocity model developed using nonlinear asymptotic coupling theory, *J. Geophys. Res.*, *101*, 22,245–22,272, 1996.

Lithgow-Bertelloni, C., and M. A. Richards, Cenozoic plate driving forces, *Geophys. Res. Lett.*, *22*, 1317–1320, 1995.

Lithgow-Bertelloni, C., and M. A. Richards, The dynamics of Cenozoic and Mesozoic plate motions, *Rev. Geophys.*, *36*, 27–78, 1998.

Lithgow-Bertelloni, C., M. A. Richards, Y. Ricard, R. J. O'Connell, and D. C. Engebretson, Toroidal-poloidal partitioning of plate motions since 120 Ma, *Geophys. Res. Lett.*, *20*, 375–378, 1993.

Marsh, J. G., et al., The GEM-T2 gravitational model, *J. Geophys. Res.*, *95*, 22,043–22,071, 1990.

Matthews, R., Inertia: Does empty space put up the resistance?, *Science*, *263*, 612–613, 1994.

McKenzie, D. P., Speculations on the consequences and causes of plate motions, *Geophys. J. R. Astron. Soc.*, *18*, 1–18, 1969.

McKenzie, D. P., Surface deformation, gravity anomalies and convection, *Geophys. J. R. Astron. Soc.*, *48*, 211–238, 1977.

McKenzie, D. P., and N. O. Weiss, Speculations on the thermal and tectonic history of the Earth, *Geophys. J. R. Astron. Soc.*, *42*, 131–174, 1975.

Molnar, P., and D. Grey, Subduction of continental lithosphere: Some constraints and uncertainties, *Geology*, *7*, 58–62, 1979.

Molnar, P., D. Freedman, and J. S. Shih, Lengths of intermediate and deep seismic zones and temperatures in downgoing slabs of lithosphere, *Geophys. J. R. Astron. Soc.*, *56*, 41–54, 1979.

Morelli, A., and A. M. Dziewonski, Topography of the core-mantle boundary and lateral homogeneity of the liquid core, *Nature*, *325*, 678–683, 1987.

Morgan, W. J., Gravity anomalies and convection currents, 1, A sphere and cylinder sinking beneath the surface of a viscous fluid, *J. Geophys. Res.*, *70*, 6175–6187, 1965.

Moritz, H., Geodetic Reference System 1989, *Bull. Géod.*, *54*, 395–405, 1980.

Moritz, H., *The Figure of the Earth: Theoretical Geodesy and the Earth's Interior*, 279 pp., Herbert Wichmann Verlag, Karlsruhe, Germany, 1990.

Munk, W. H., and G. J. F. MacDonald, Continentality and the gravitational field of the Earth, *J. Geophys. Res.*, *65*, 2169–2172, 1960.

Nakiboglu, S. M., Hydrostatic theory of the Earth and its mechanical implications, *Phys. Earth Planet. Inter.*, *28*, 302–311, 1982.

Nerem, R. S., B. G. Bills, and J. B. McNamee, A high-resolution gravity model for Venus: GVM-1, *Geophys. Res. Lett.*, *20*, 599–602, 1993.

Nordtvedt, K., From Newton's moon to Einstein's moon, *Phys. Today*, 26–31, May 1996.

O'Connell, R. J., and B. Hager, On the thermal state of the Earth, in *Physics of the Earth's Interior*, edited by A. Dziewonski and E. Boschi, pp. 270–317, North-Holland, New York, 1980.

O'Keefe, J. A., and W. M. Kaula, Stress differences and the reference ellipsoid, *Science*, *142*, 382, 1963.

Oxburgh, E. R., and D. L. Turcotte, Mechanisms of continental drift, *Rep. Prog. Phys.*, *41*, 1249–1312, 1978.

Parker, R. L., and D. W. Oldenburg, Thermal models of ocean ridges, *Nature*, *242*, 137–139, 1973.

Parsons, B., and S. Daly, The relationship between surface topography, gravity anomalies and the temperature structure of convection, *J. Geophys. Res.*, *88*, 1129–1144, 1983.

Parsons, B. E., and D. P. McKenzie, Mantle convection and the thermal structure of the plates, *J. Geophys. Res.*, *83*, 4485–4496, 1978.

Parsons, B., and J. G. Sclater, An analysis of the variation of ocean floor bathymetry and heat flow with age, *J. Geophys. Res.*, *82*, 803–827, 1977.

Pekeris, C. L., Thermal convection in the interior of the Earth, *Mon. Not. R. Astron. Soc.*, suppl., *3*, 343–367, 1935.

Rapp, R. H., Geos 3 data processing for the recovery of geoid undulations and gravity anomalies, *J. Geophys. Res.*, *84*, 3784–3792, 1979.

Rauch, H., Neutron interferometry, *Science*, *262*, 1384–1385, 1993.

Regalado, A., G Whizzes disagree, *Science*, *268*, 640–641, 1995.

Ricard, Y., G. Spada, and R. Sabadini, Polar wandering of a dynamic planet, *Geophys. J. Int.*, *113*, 284–298, 1993a.

Ricard, Y., M. Richards, C. Lithgow-Bertelloni, and Y. Le Stunff, A geodynamic model of mantle density heterogeneity, *J. Geophys. Res.*, *98*, 21,895–21,909, 1993b.

Richards, M. A., and B. H. Hager, Geoid anomalies in a dynamic Earth, *J. Geophys. Res.*, *89*, 5987–6002, 1984.

Richter, F., Dynamical models for sea floor spreading, *Rev. Geophys.*, *11*, 223–287, 1973.

Richter, F. M., and B. E. Parsons, On the interaction of two scales of convection in the mantle, *J. Geophys. Res.*, *80*, 2529–2541, 1975.

Sandwell, D. T., and W. H. F. Smith, Marine gravity anomaly from Geosat and ERS 1 satellite altimetry, *J. Geophys. Res.*, *102*, 10,039–10,054, 1997.

Schubert, G., C. Froidevaux, and D. A. Yuen, Oceanic lithosphere and asthenosphere: Thermal and mechanical structures, *J. Geophys. Res.*, *81*, 3525–3540, 1976.

Schubert, G., D. A. Yuen, C. Froidevaux, L. Fleitout, and M. Souria, Mantle circulation with partial shallow return flow: Effects on stresses in oceanic plates and topography of the sea floor, *J. Geophys. Res.*, *83*, 745–758, 1978.

Sincell, M., Firming up the case for a flat cosmos, *Science*, *285*, 1831, 1999.

Sleep, N. H., Hotspots and mantle plumes: Some phenomenology, *J. Geophys. Res.*, *95*, 6715–6736, 1990.

Smith, D., F. J. Lerch, R. S. Nerem, M. T. Zuber, G. B. Patel, S. K. Fricke, and F. G. Lemoine, An improved gravity model for Mars: Goddard Mars Model 1, *J. Geophys. Res.*, *98*, 20,871–20,889, 1993.

Stephen, R., Seismic network management structure, *Oceanus*, *41*(1), 34, 1998.

Su, W.-J., R. L. Woodward, and A. Dziewonski, Degree 12 model of shear velocity heterogeneity in the mantle, *J. Geophys. Res.*, *99*, 6945–6980, 1994.

Taylor, J. H., and J. M. Weisberg, Further experimental tests of relativistic gravity using the binary pulsar PSR−1913+16, *Astrophys. J.*, *345*, 434–450, 1989.

Thoraval, C., P. Machetal, and A. Cazenave, Locally layered convection inferred from dynamic models of the Earth's mantle, *Nature*, *375*, 777–779, 1995.

Torge, W., *Gravimetry*, Walter de Gruyer, 465 pp., Berlin, 1989.

van der Hilst, R. D., S. Widiyantoro, and E. R. Engdahl, Evidence for deep mantle circulation from global tomography, *Nature*, *386*, 578–584, 1997.

van der Klis, M., The buzz of general relativity, *Science*, *285*, 1499–1500, 1999.

Wessel, P., and W. H. F. Smith, Free software helps map and display data, *Eos Trans. AGU*, *72*, 441, 1991.

Witten, E., Duality, spacetime and quantum mechanics, *Phys. Today*, 28–33, May 1997.

Woodhouse, J. H., and A. M. Dziewonski, Seismic modeling of the Earth's large-scale three-dimensional structure, *Philos. Trans. R. Soc. London, Ser. A*, *328*, 291–308, 1989.

C. Bowin, Department of Geology and Geophysics, Woods Hole Oceanographic Institution, Woods Hole, MA 02543. (cbowin@whoi.edu)